Kinematic response of flexible suction caissons for offshore wind turbines to vertically incident shear waves

Jacob D. R. Bordón[*], Cristina Medina, Juan C. Galván, and Luis A. Padrón

Instituto Universitario de Sistemas Inteligentes y Aplicaciones Numéricas en Ingeniería (SIANI)
Universidad de Las Palmas de Gran Canaria (ULPGC)
Edificio Central del Parque Científico y Tecnológico, Campus Universitario de Tafira
35017 Las Palmas de Gran Canaria

This is a preprint of a paper published in Ocean Engineering, Volume 326, 120750, 15 May 2025. To access the final edited and published work see `https://doi.org/10.1016/j.oceaneng.2025.120750`.

Abstract

This paper presents the translational and rotational kinematic interaction factors of flexible suction caissons considering structural and soil properties relevant to the seismic analysis of offshore wind turbines. Kinematic stresses developed along the foundation skirt are also presented and analyzed. The parametric analysis performed considers four height–to–diameter ratios between 0.5 and 2, three skirt thickness–to–diameter ratios between 0.5% to 2.0%, and four different relevant skirt–soil stiffness ratios for sand soils. The foundations are assummed to be founded in homogenous and non-homogeneous soils, and they are considered to be subjected to vertically–incident shear waves. The kinematic response of the foundations is computed through an advanced boundary element – finite element coupled numerical model. It is found that the kinematic interaction factors are fundamentally independent of the skirt–soil stiffness ratio. It is also found that the general pattern of the kinematic interaction factors is analogous to that of piles, and that significant filtering of the seismic input motions can be observed. Results are presented in ready–to–use dimensionless plots. Regarding kinematic stresses, shell-like or beam-like behaviour is observed depending on height–to–diameter ratio of the skirt.

Keywords: *Suction Caissons; Bucket; Foundations; Offshore Wind Turbines; Kinematic interaction; Kinematic forces; Earthquake Engineering*

1 Introduction

The knowledge of the kinematic response of a foundation subjected to incoming seismic waves is a prerequisite in the framework of the analysis of the seismic response of structures by substructuring techniques and the three–step method [1]. This kinematic response is usually encapsulated in the harmonic displacements and rotations experienced by the foundation at the point of connection with the upper structure, relative to a measure of the intensity of the incoming planar seismic waves, generally the ground motions that would be registered at ground surface in the absence of the foundation (free–field response).

Such information is usually provided in the form of frequency–dependent translational and rotational kinematic interaction factors that can later be employed to filter any specific seismic signal to be used in the analysis of the structural response. Kinematic interaction factors for foundations typologies such as footings (e.g. [2, 3]), single piles (e.g. [4–9]), pile groups (e.g. [5, 10–15]) or monopiles for offshore wind turbines (e.g. [16–19]) have received a great deal of attention for a long time, so they are readily available in the literature for many different configurations. The structural forces produced in the foundation (especially in the case of piles) by the action of the incoming seismic waves is another side of the problem of great significance, and it has also been researched in depth, considering single piles (e.g. [20–25]), pile groups (e.g. [26, 27]) or both (e.g. [28–31]).

The kinematic response of suction caissons, on the contrary, has not been studied in detail. Although the impedance problem of this type of foundations has been addressed in numerous papers (see for instance [32–44]), general kinematic interaction factors for suction caissons are not available.

---

[*] Corresponding author: ORCID; `jacobdavid.rodriguezbordon@ulpgc.es`

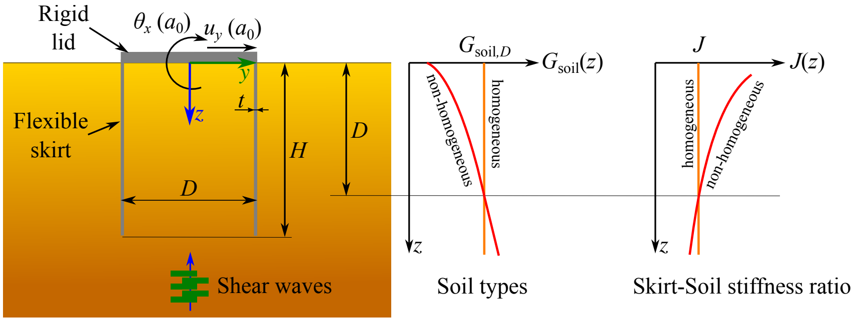

Figure 1: Problem definition. Sectional view.

	Skirt steel	Soil
Shear Modulus G [GPa]	80	See Eq. 1
Density ρ [kg/m^3]	7850	2000
Poisson's ratio μ	0.3	0.4
Damping ratio ξ	2%	5%

Table 1: Steel and soil material constants

For this reason, this study aims to present and analyze the translational and rotational kinematic interaction factors of suction caissons subjected to vertically incident planar shear waves. A wide range of configurations compatible with the case of the foundations for offshore wind turbines are considered. Likewise, the kinematic stress resultants that develop within the skirt of the foundation due to the action of the seismic waves are studied.

Section 2 presents in detail the problem at hand and the ranges of material and geometrical properties that were considered. Afterwards, section 3 describes and verify the methodology that has been employed for computing the kinematic response of the foundation. Then, section 4 presents the computed kinematic interaction factors in ready–to–use frequency–dependent dimensionless plots from which the translational and the rotational factors can be obtained for specific cases. This section also analyses different interesting patterns that can be observed in the response. The kinematic stress resultants along the bucket skirt that can be observed in the foundations are also discussed in a different subsection.

2 Problem definition

The foundation under study is a steel suction caisson composed by a flexible thin skirt of thickness t, depth H and diameter D, and a strongly stiffened lid of diameter D, as shown in Fig. 1. Thus, for the purpose of studying the kinematic response of the system, the lid is considered rigid and massless, and it is assumed to be rigidly welded to the skirt around all its perimeter. These assumptions have been largely used for this type of foundations as well as monopiles in seismic analysis, see e.g. [17, 33, 41]. The soil is modelled as a viscoelastic halfspace that can be either homogenous or depth-dependent non-homogeneous, with a soil shear modulus $G_{\text{soil}}(z)$ defined as

$$G_{\text{soil}}(z) = G_{\text{soil},D}\left(\frac{z+0.2}{D+0.2}\right)^{\beta} \tag{1}$$

where z is the depth within the soil measured from ground surface, $G_{\text{soil},D}$ is the shear modulus of the soil assumed at a depth $z = D$, and β is the parameter that governs the type of profile [45], with $\beta = 0$ leading to a constant value (homogeneous soil) and $\beta = 0.5$ leading to an exponential continuous (non-homogenous) profile for which the shear modulus at ground surface is small but not zero. The rest of the material properties are those presented in Table 1. Hysteretic material damping is introduced in the model through complex–valued stiffnesses of the type $G = \text{Re}[G](1 + 2\text{i}\xi)$, where $\text{i} = \sqrt{-1}$. In all cases, the structure and the soil are considered to be in close contact, and no sliding or separation are allowed. Thus, perfectly welded contact conditions are assumed between soil and skirt, and between the lower face of the lid and the surface of the soil.

The foundation is assumed to be subjected to vertically–incident planar shear waves that produce a unitary horizontal displacement at free–field ground surface. The response of the foundation under

Parameter	Adopted values
Skirt–soil stiffness ratio (J)	10, 25, 100 and 250
Soil type	homogeneous ($\beta = 0$) non–homogeneous ($\beta = 0.5$)
Slenderness ratio (H/D)	0.25, 0.5, 1.0 and 2.0
Thickness ratio (t/D)	0.5%, 1.0% and 2.0%

Table 2: Parameter values adopted for the parametric study

the impinging seismic waves is presented in terms of translational and rotational kinematic interaction factors [4, 5] respectively defined as

$$I_u\left(a_0\right) = \frac{u_y^{\text{lid}-\text{center}}\left(a_0\right)}{u_y^{\text{free}-\text{field}}\left(a_0\right)} \quad \text{and} \quad I_\theta\left(a_0\right) = \frac{\theta_x^{\text{lid}-\text{center}}\left(a_0\right)\cdot D/2}{u_y^{\text{free}-\text{field}}\left(a_0\right)} \tag{2}$$

where $u_y^{\text{free}-\text{field}}\left(a_0\right)$ is the frequency–dependent free–field displacement at ground surface produced by the incoming seismic shear waves, $u_y^{\text{lid}-\text{center}}\left(a_0\right)$ is the frequency–dependent horizontal displacement computed at the center of the lid, $\theta_x^{\text{lid}-\text{center}}\left(a_0\right)$ is the frequency–dependent rotation measured at the rigid lid, and $a_0 = \omega \cdot R/c_{s,D}$ is the dimensionless frequency, with ω being the angular frequency, $R = D/2$ and $c_{s,D}$ the soil shear wave velocity at $z = D$.

The kinematic response of such type of foundation is computed for a wide range of geometrical ratios that are representative of the dimensions of suction caissons designed for offshore wind turbines. The specific values that have been considered in this parametric study are presented in Table 2. Here, the range of relative stiffnesses between skirt and soil (primarily due to the possible different properties of the soils) is represented by a dimensionless skirt–soil stiffness ratio defined as [46, 47]

$$J = \frac{G_{\text{skirt}}}{G_{\text{soil},D}}\frac{t}{D} \tag{3}$$

where G_{skirt} is the shear modulus of the skirt material (steel in this case). Since the value of J is established at depth $z = D$ in order to being able to compare homogeneous and non-homogeneous soils, a depth-dependent skirt–soil stiffness ratio is actually present in non-homogeneous soil cases, which for the defined soil profile is

$$J(z) = J\left(\frac{z+0.2}{D+0.2}\right)^{-\beta} \tag{4}$$

leading to quite greater $J(z) > J$ for depths $z < D$, and somewhat smaller $J(z) < J$ for depths $z > D$, as shown in Fig. 1. This way, the results can be presented, mostly, in terms of dimensionless parameters, so that they can be employed to a wide range of particular cases. Given the fixed adopted value for the shear modulus of the steel given in Table 1, the values presented in Table 2 are representative of soils with shear wave velocities between 28 m/s ($J = 250$) and 283 m/s ($J = 10$). Fig. 2 illustrates the geometry of the studied typologies considering the four different diameter–to–embdement ratios under consideration. The parametric study represented by the values of the table give rise to a total of 96 different configurations. All the results for homogeneous cases are fully generalizable as the problem can be fully written in dimensionless terms. However, the results for non-homogeneous cases are not fully generalizable due to the soil profile defined, which requires defining the diameter, or the ratio between the shear modulus at the free-surface and the shear modulus at depth $z = D$. In the present paper, all results for the non-homogeneous soil assume $D = 12$ m (intermediate bucket diameter), which leads to $G_{\text{soil}}(0) = 0.128 \cdot G_{\text{soil},D}$.

3 Methodology

The methodology used to tackle the previously defined problem is based on a coupled model of boundary elements and finite elements developed within MultiFEBE [48]. In particular, a horizontally layered elastic half-space Green's function [49] has been introduced in the code, so that neither free-surface nor interface between layers need to be discretized. In the following, such model is described.

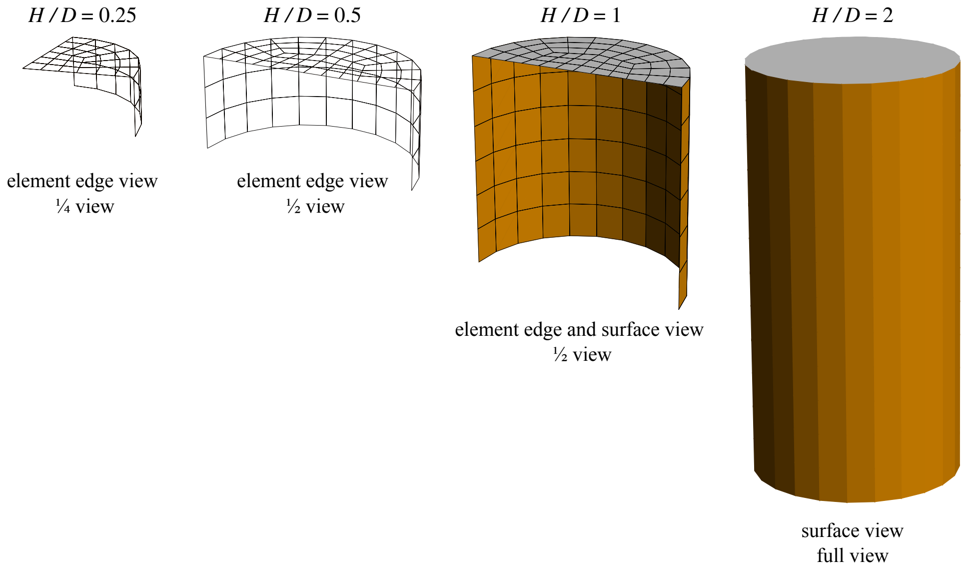

Figure 2: Suction caisson geometries and meshes

3.1 Skirt and lid modeling

The whole foundation is modeled using shell finite elements, where the skirt is a cylindrical steel shell of thickness t, depth H and diameter D, and the lid is considered as a simple circular plate of diameter D with modified material properties which approximates a massless and rigid lid (shear modulus of $10^6 \cdot G_{\text{skirt}}$ and null density). Both are perfectly welded together with continuity of displacements and rotations.

Locking-free MITC Reissner-Mindlin shell finite elements [50] are used. The usual element equilibrium equation for time harmonic analyses can be written in matrix form as [51]

$$\tilde{\mathbf{K}}^{(e)}(\omega) \cdot \mathbf{a}^{(e)}(\omega) - \mathbf{Q}^{(e)} \cdot \mathbf{f}^{(e)}(\omega) = \mathbf{q}^{(e)}(\omega) \tag{5}$$

where ω is the angular frequency, $\tilde{\mathbf{K}}^{(e)}(\omega) = \mathbf{K}^{(e)} - \omega^2\mathbf{M}^{(e)}$ is the element time–harmonic stiffness matrix with $\mathbf{K}^{(e)}$ and $\mathbf{M}^{(e)}$ respectively being the stiffness and mass matrices, $\mathbf{a}^{(e)}(\omega)$ is the vector of element degrees of freedom, $\mathbf{Q}^{(e)}$ is the matrix which transforms mid-surface distributed forces $\mathbf{f}^{(e)}(\omega)$ into equivalent nodal loads, and $\mathbf{q}^{(e)}(\omega)$ is the element equilibrating load vector. More specifically, for an element e with N nodes

$$\mathbf{a}^{(e)} = \left(\mathbf{a}_1^{(e)}, \ldots, \mathbf{a}_N^{(e)}\right)^T = \left(\mathbf{a}^{(n_1)}, \ldots, \mathbf{a}^{(n_N)}\right)^T \tag{6}$$

$$\mathbf{f}^{(e)} = \left(\mathbf{f}_1^{(e)}, \ldots, \mathbf{f}_N^{(e)}\right)^T = \left(\mathbf{f}^{(n_1)}, \ldots, \mathbf{f}^{(n_N)}\right)^T \tag{7}$$

and, for a given node n

$$\mathbf{a}^{(n)} = \left(u_x^{(n)}, u_y^{(n)}, u_z^{(n)}, \theta_x^{(n)}, \theta_y^{(n)}, \theta_z^{(n)}\right)^T \quad \text{(6 DOF shell node with global rotations)} \tag{8}$$

$$\mathbf{a}^{(n)} = \left(u_x^{(n)}, u_y^{(n)}, u_z^{(n)}, \alpha^{(n)}, \beta^{(n)}\right)^T \quad \text{(5 DOF shell node with local rotations)} \tag{9}$$

$$\mathbf{f}^{(n)} = \left(f_x^{(n)}, f_y^{(n)}, f_z^{(n)}\right)^T \quad \text{(forces per unit area)} \tag{10}$$

where nodal displacements, rotations and forces are all frequency-dependant, but the dependency is omitted in the notation for the sake of brevity. When modeling shells in typical structures, distributed forces $\mathbf{f}^{(e)}$ are prescribed. However, in the present model they remain as active degrees of freedom due to the coupling to boundary elements (representing the soil-lid interaction loads) or body surface load elements (representing the soil-skirt interaction loads).

3.2 Soil modeling

The soil is modeled using the Boundary Element Method. A starting point of the method is the displacement-based boundary integral equation [52]

$$c_{lk}^{(i)}u_k^{(i)} + \int\limits_{\Gamma} t_{lk}^* u_k \, \mathrm{d}\Gamma = \int\limits_{\Gamma} u_{lk}^* t_k \, \mathrm{d}\Gamma + \int\limits_{\Omega} u_{lk}^* b_k \, \mathrm{d}\Omega, \quad l,k = 1,2,3 \equiv x,y,z \tag{11}$$

where Einstein summation is implied, and $c_{lk}^{(i)}$ is the free-term. It relates body loads $b_k = b_k(\omega)$ throughout the domain Ω, displacements $u_k = u_k(\omega)$ and tractions $t_k = t_k(\omega)$ throughout the boundary $\Gamma = \partial\Omega$ and the displacement $u_k^{(i)} = u_k^{(i)}(\omega)$ at the collocation point of the point load. In this equation, the Green's function in terms of displacements is $u_{lk}^* = u_{lk}^*(\omega)$ and in term of tractions is $t_{lk}^* = \sigma_{lkj}^*(\omega)n_j$, where the first index l is related to the load direction, the second index k is related to the observation direction, and n_j is the outward unit normal ($j = 1,2,3$ is a dummy index). A Green's function for a horizontally layered elastic half-space [49] is used in this work. Since the considered Green's function already considers the stratigraphy and it also fulfill the traction-free conditions at the free-surface, integrals along Γ are null except along the soil-lid interface when the lid is considered to be in contact with the soil, and even in that case the integral including t_{lk}^* is null since this is also null by definition. Body loads are usually a prescribed load, but here they act as active degrees of freedom together with their displacements. This way, boundary integral equations which model the soil can be written as

$$c_{lk}^{(i)}u_k^{(i)} = \int\limits_{\Gamma_{\text{lid}}} u_{lk}^* t_k \, \mathrm{d}\Gamma + \int\limits_{\Pi_{\text{skirt}}} u_{lk}^* b_k \, \mathrm{d}\Pi \tag{12}$$

where Γ_{lid} represents the soil-lid interface and Π_{skirt} represents the soil-skirt interface.

The discretization of the previous equation follows the usual procedure [52]. Two-dimensional isoparametric Lagrange elements are used for both the soil-lid (boundary elements) and soil-skirt (surface body load elements). In the first case, the degrees of freedom are the soil displacements u_k and tractions t_k along the soil-lid interface. In the second case, the degrees of freedom are the soil displacements u_k and body loads b_k along the soil-skirt interface.

The collocation procedure consists of using nodal collocation at all nodes except at nodes located along the boundary of the surface, where non-nodal collocation is applied, see e.g. [34].

3.3 Soil-lid and soil-skirt coupling

A conforming mesh between soil boundary or body load elements and suction caisson shell finite elements is used, where a node-node coupling between both is considered. Welded contact conditions are imposed via displacement compatibility and equilibrium at the interface:

- Each soil boundary element node n_{BE} coincident with a lid shell finite element node n_{FE} requires

  $$u_k^{(n_{\text{BE}})} = u_k^{(n_{\text{FE}})} \tag{13}$$
  $$f_k^{(n_{\text{FE}})} = -t_k^{(n_{\text{BE}})} \tag{14}$$

  where $k = 1,2,3 \equiv x,y,z$. Then $u_k^{(n_{\text{FE}})}$ and $t_k^{(n_{\text{BE}})}$ remain as the active degrees of freedom in the linear system of equations.

- Each soil body surface load element node n_{LE} coincident with a skirt shell finite element node n_{FE} requires

  $$u_k^{(n_{\text{LE}})} = u_k^{(n_{\text{FE}})} \tag{15}$$
  $$f_k^{(n_{\text{FE}})} = -b_k^{(n_{\text{LE}})} \tag{16}$$

  and then $u_k^{(n_{\text{FE}})}$ and $b_k^{(n_{\text{LE}})}$ remain as the active degrees of freedom in the linear system of equations.

3.4 Incident field

The foundation is assumed to be subjected to plane time-harmonic SH waves that propagate vertically through the stratified soil and produce motions along the y-direction. Therefore, the displacement field within each layer is of the form [52–54]

$$u_y^{\text{free-field}}(z,\omega) = A_j \mathrm{e}^{\mathrm{i}k_j z} + B_j \mathrm{e}^{-\mathrm{i}k_j z} \tag{17}$$

where A_j and B_j are the amplitudes of the waves ascending and descending through layer j and $k_j = \omega/c_j$ is its wavenumber. Coefficients A_j and B_j are computed in each case considering unitary horizontal displacements at the free surface ($z = 0$), zero stresses at that free surface, and compatibility and equilibrium at the interfaces between layers. In the case of the homogeneous soil, the soil is modeled as a half space, and the expression above simplifies. In the case of the inhomogeneous soil, the incident field is approximated by considering a sufficiently large number of layers. This incident field is introduced into the soil boundary element equations by decomposing the total field into the free-field and the scattered field

$$u_y(z,\omega) = u_y^{\text{free-field}}(z,\omega) + u_y^{\text{scattered}}(z,\omega) \tag{18}$$

and then the scattered field $u_y(\omega) - u_y^{\text{free-field}}(\omega)$ is the one used in the boundary integral equations, see e.g. [52].

3.5 Verification

In this section, the developed methodology is verified by comparing it against reference results. For this purpose, the well-known pile kinematic response results from [11] are considered. In this reference, the kinematic interaction factors of free-head floating circular piles in homogeneous soils are obtained. Results assume fixed dimensionless parameters such as Poisson's ratios of the soil ($\nu_{\text{soil}} = 0.4$) and pile ($\nu_{\text{pile}} = 0.25$), hysteretic damping ratio ($\xi_{\text{soil}} = 0.05$), and soil density to pile density ratio ($\rho_{\text{soil}}/\rho_{\text{pile}} = 0.7$), while different length to diameter ratios ($H/D = 20$, $H/D = 40$) and pile Young's modulus to soil Young's modulus ratios ($E_{\text{pile}}/E_{\text{soil}} = 1000$, $E_{\text{pile}}/E_{\text{soil}} = 10000$) are considered. Given that the present methodology is developed for cylindrical skirts modelled using shells, an equivalence between a solid circular cross section and a circular hollow cross section must be established. Given that the pile is mainly subjected to bending, the mechanical equivalence between both is established by imposing equal bending stiffness and equal translational inertia

$$E_{\text{pile}} \frac{\pi D^4}{64} = E_{\text{skirt}} \frac{\pi D^3 t}{8} \tag{19}$$

$$\rho_{\text{pile}} \frac{\pi D^2}{4} = (\rho_{\text{skirt}} - \rho_{\text{soil}}) \pi D t + \rho_{\text{soil}} \frac{\pi D^2}{4} \tag{20}$$

where the internal soil bending stiffness is neglected, and the overlapping of masses due to the assumed shell-soil interaction modelling is taken into account. This allows to write the relationship between stiffnesses ratios as

$$J = \frac{1}{8} \frac{1 + \nu_{\text{soil}}}{1 + \nu_{\text{skirt}}} \frac{E_{\text{pile}}}{E_{\text{soil}}} \tag{21}$$

and between density ratios as

$$\frac{\rho_{\text{skirt}}}{\rho_{\text{soil}}} = \frac{1}{4} \left(1 + \frac{\rho_{\text{pile}}}{\rho_{\text{soil}}}\right) \frac{1}{t/D} \tag{22}$$

Therefore, by establishing any values to D, E_{soil} and ρ_{soil}, the rest of the parameters are found by using the previous dimensionless relationships. Figure 3 shows the absolute value of the translational and rotational kinematic interaction factors given by [11] together with those obtained from the present methodology. A close agreement of the present method is observed.

4 Results

4.1 Kinematic interaction factors

Figures 5 and 6 present the translational and rotational kinematic interaction factors obtained in the case of a homogeneous soil. Each figure presents eight subplots, with the real parts on the left, the imaginary

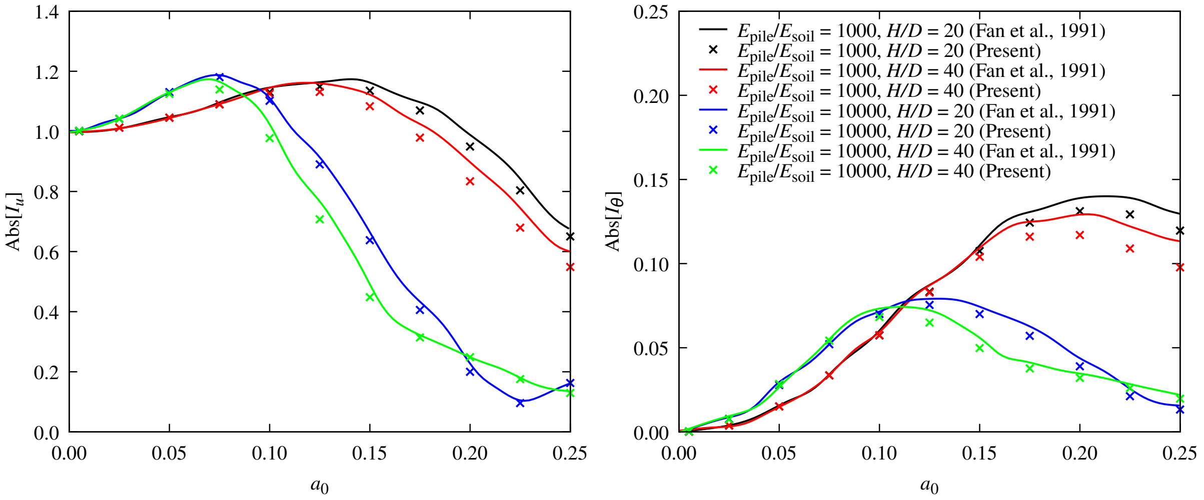

Figure 3: Comparison of I_u and I_θ between [11] and the present methodology for homogeneous soil. Other dimensionless parameters are $\nu_{\text{soil}} = 0.4$, $\nu_{\text{pile}} = 0.25$, $\xi_{\text{soil}} = 0.05$, $\rho_{\text{soil}}/\rho_{\text{pile}} = 0.7$.

parts on the right, and one row per value of the embedment ratio H/D. The dimensionless factors are presented as a function of the dimensionless frequency a_0, and the curves that correspond to different values of the skirt–soil stiffness ratio J are presented in different colors in each subplot.

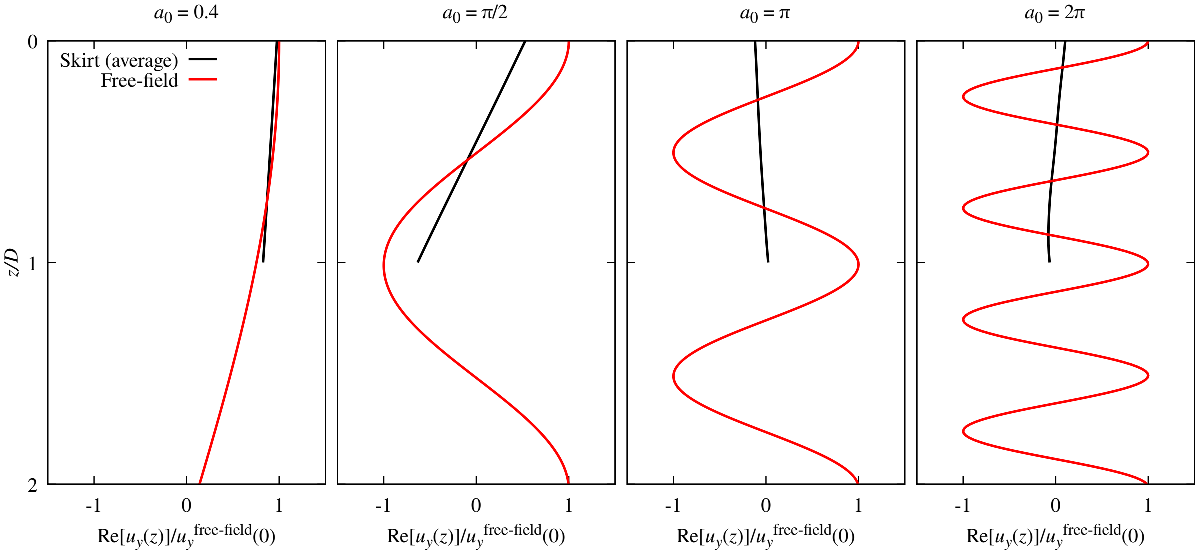

Figure 4: Horizontal displacements u_y of the free-field and the skirt along the depth at characteristic frequencies. Case: $H/D = 1$, $J = 100$, $t/D = 1\%$, homogeneous soil.

The general characteristics of the kinematic interaction factors of these suction caissons are, even with very small embedment ratios, analogous to those already well known for piles (see for instance Fig.3a in [12] for the translational kinematic interaction factors). The results can be explained by examining Figures 5-6 together with Fig. 4, which illustrates the physical phenomena for a specific case by showing the real part of the horizontal displacements of the free-field and the average kinematics of the skirt along the depth.

At very low frequencies, i.e. very large soil wavelengths with respect to the foundation depth, the foundation mainly translates in phase with the free-field, as it can be observed from the first column of Fig. 4 ($a_0 = 0.4$). Thus, at this very low–frequency part, the real part of the translational kinematic interaction factors start from unit values and the rotational ones start from zero, while the imaginary parts of both kinematic interaction factors start from zero. That means that the seismic excitation is not being filtered by the foundation.

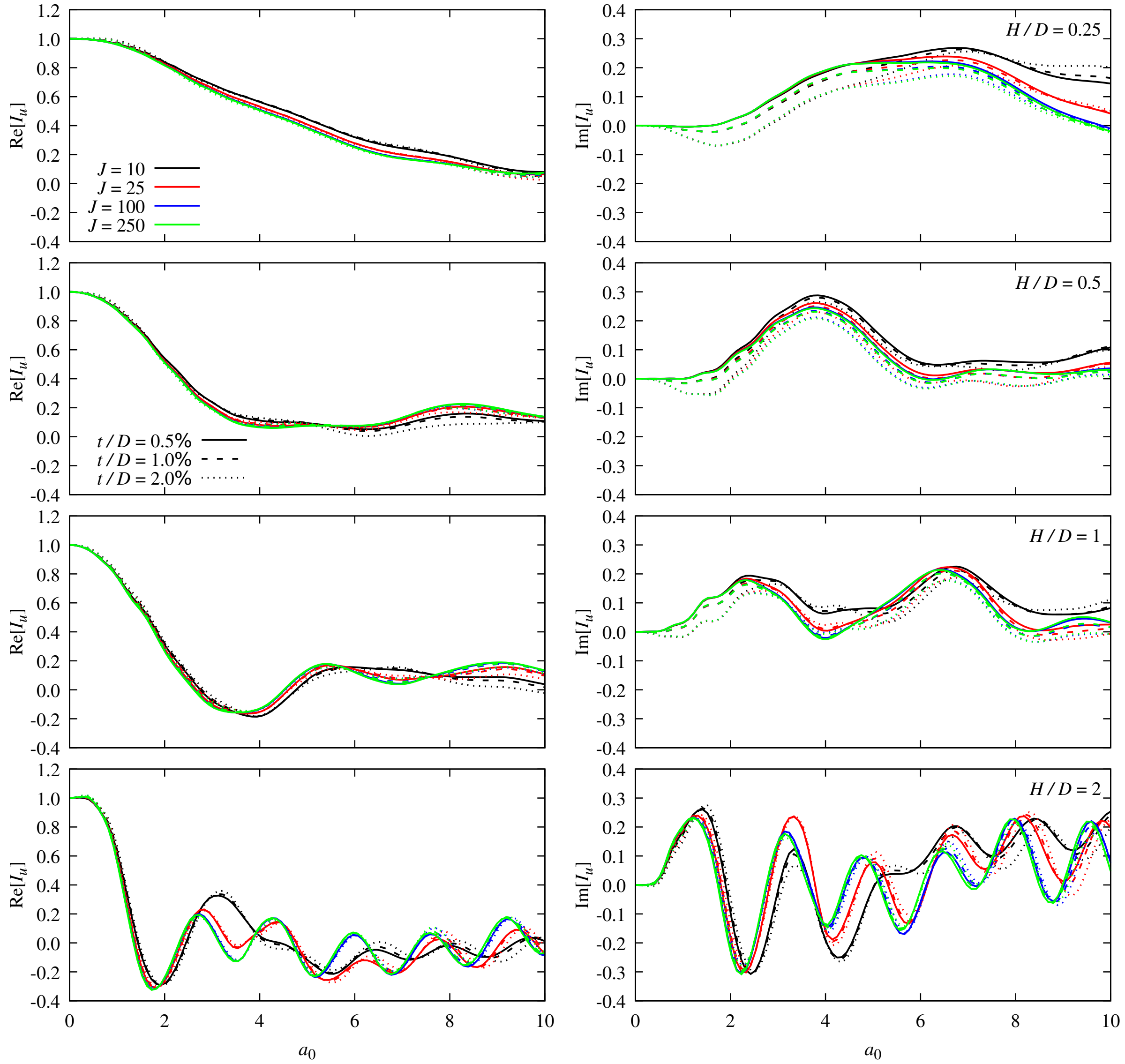

Figure 5: Translational kinematic interaction factors. Homogeneous soil

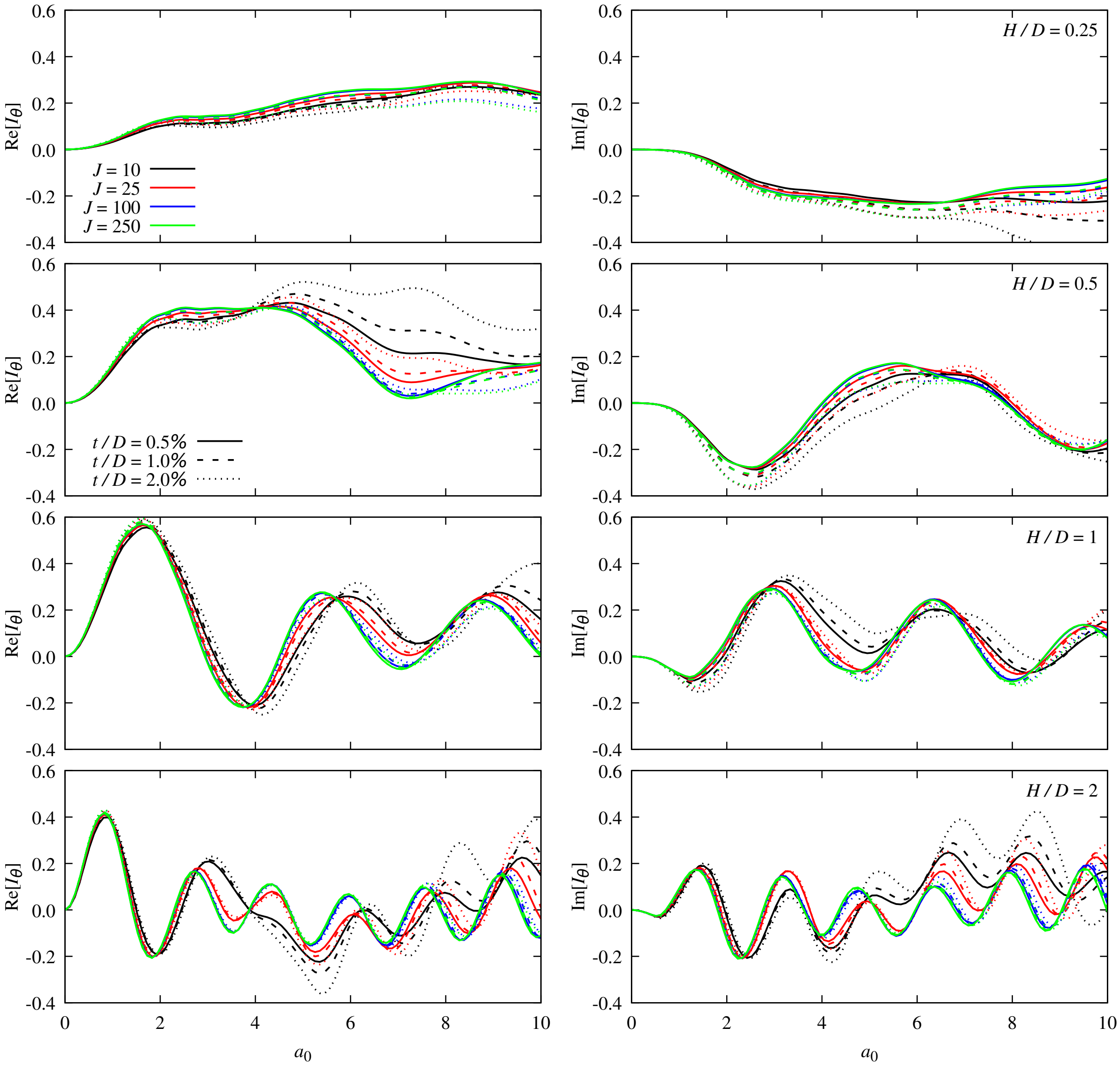

Figure 6: Rotational kinematic interaction factors. Homogeneous soil

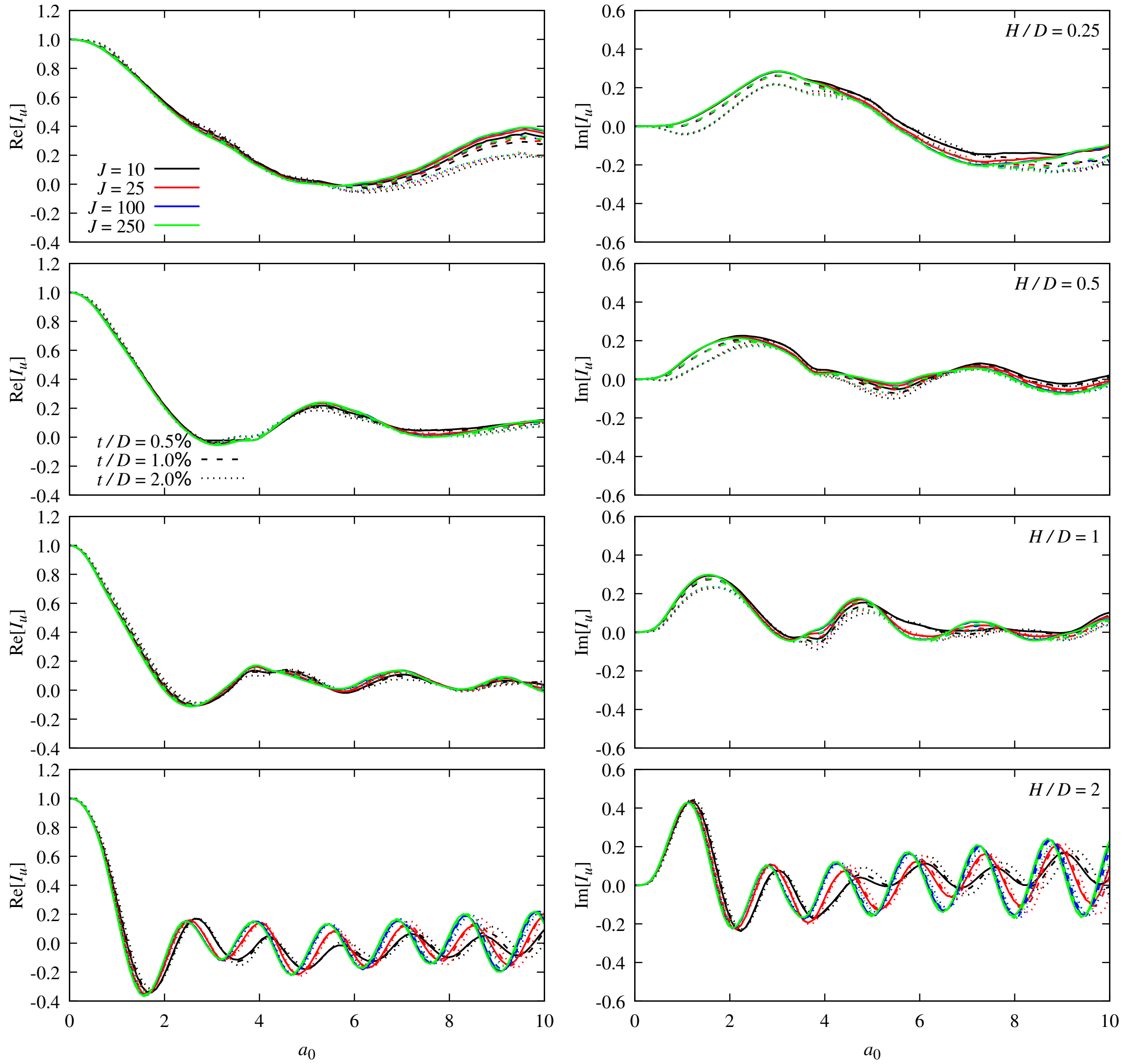

Figure 7: Translational kinematic interaction factors. Non-homogeneous soil

Then, as the frequency increases and the foundation depth encompasses more than one-quarter of the soil wavelength, the foundation still translates in phase with the free-field but with a smaller amplitude, and it starts to rotate since the displacements of the free-field at the free-surface and at the foundation bottom start to be out of phase. That means that the real part of the translational kinematic interaction factors decreases and the rotational ones increases with the frequency, while the imaginary parts of both factors increase. The first peak in the real part of the rotational kinematic interaction factor occurs at the frequency when one-half of the soil wavelength coincides with the foundation depth because free-surface displacement are 180 degrees out-of-phase. This can be observed from the second column of Fig. 4 ($a_0 = \pi/2$), which in general occurs approximately at $a_0 = (\pi/2)/(H/D)$.

As the frequency keeps increasing, the free-field at the bottom part of the foundation starts loosing the out of phase condition, until the frequency where the foundation depth coincides with the soil wavelength, where the free-field at the free-surface and at the foundation bottom are in phase. At this stage, the average free-field displacement along the foundation depth is approximately zero, leading to nearly zero translational interaction factors. This can be observed from the third column of Fig. 4 ($a_0 = \pi$), which in general occurs approximately at $a_0 = (\pi)/(H/D)$. Regarding the rotational interaction factors, their real parts are nearly zero while the imaginary parts reach a maximum, indicating a 90 degrees out of phase between seismic excitation and foundation rotational response at the ground surface.

The last part of higher frequencies is characterized by an irregular and alternating response around zero of both the real and the imaginary parts. Thus, the phase lag between the incident seismic wave

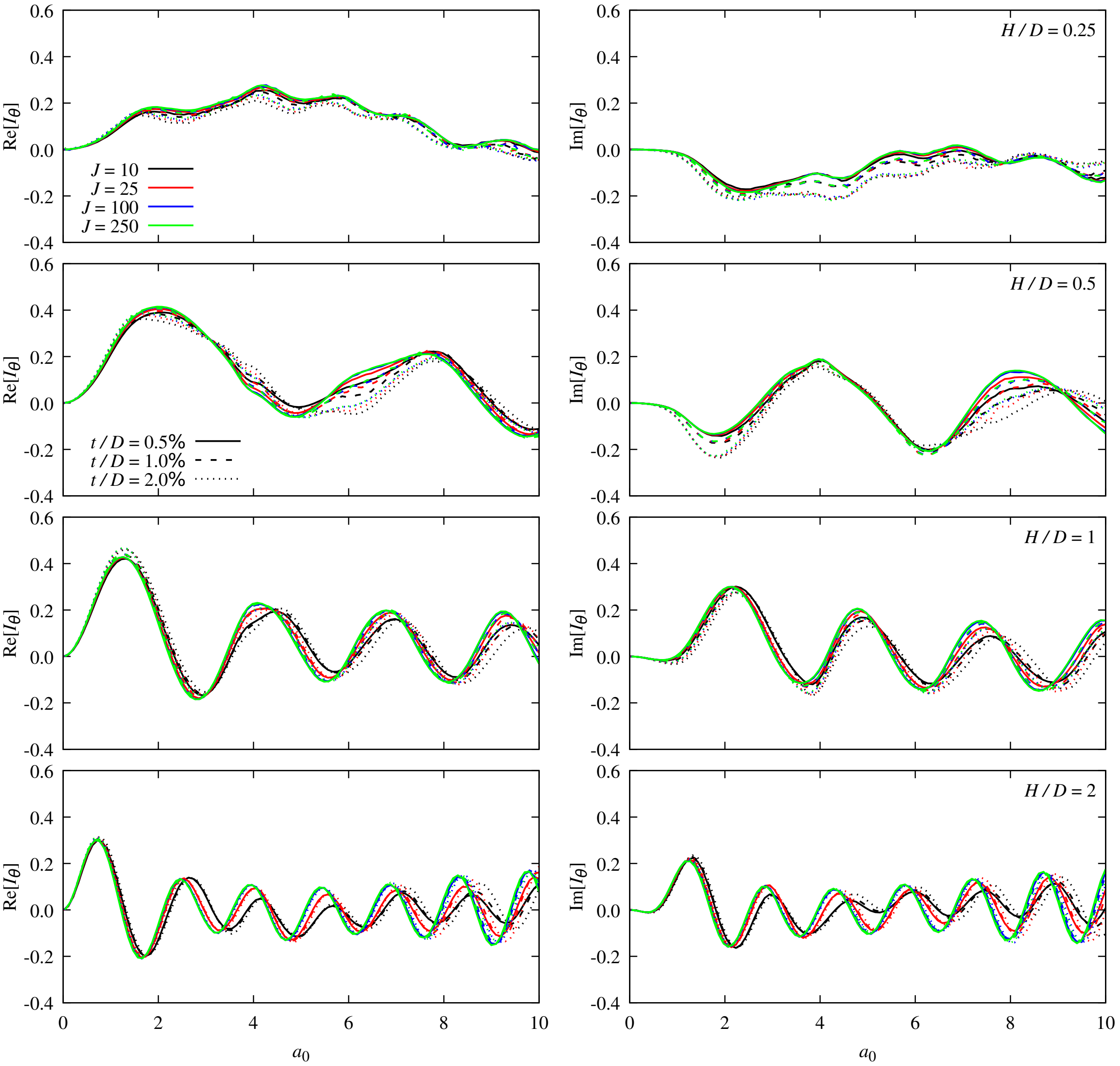

Figure 8: Rotational kinematic interaction factors. Non-homogeneous soil

and the kinematic response of the foundation will be maximum around the peaks of the imaginary part of the function in each case. It is in this high-frequency range where the relative stiffness between the cylindrical skirt and the soil starts to be noticeable, as it is illustrated in the last column Fig. 4.

Overall, it can be seen that the resulting kinematic ratios are found to be almost independent of J and t/D, within the ranges of properties considered in the study, and especially for the low frequencies. This is so because the high stiffness of the skirt of the foundation is provided by its cylindrical geometry, and the variations of the stiffness of the soil, and of the stiffness of the plate of the skirt due to the changes in thickness t, do not affect its structural behaviour at relatively low frequencies. Evidently, the high frequency response of the foundation is indeed heavily influenced by changes in structural stiffness, but the results show that, in many cases, this parameter will not be very relevant when computing the seismic response of offshore wind turbines founded on suction caissons due to the very low natural frequencies of such turbines. In relative terms, the variations of the rotational kinematic interaction factors with the skirt–soil stiffness ratio J seem to be slighly higher than those obtained for the translational factors, but this is so because the total range of the function is larger in the latter case.

Similar observations can be made with respect to the kinematic interaction factors obtained in the non-homogeneous soil, which are presented in Figs. 7 and 8. Due to the varying stiffness with depth of the non-homogenous soil, see Fig. 1, and taking into account that a_0 is based on the value of $c_{s,D}$ at $z = D$, the translational kinematic interaction factors for the non–homogeneous soils decrease more rapidly than its homogeneous counterpart. When comparing the results for homogeneous soils against the results for non-homogeneous soils, it is also observed that the relevance of the relative stiffness between skirt and soil (J and t/D) is smaller for non-homogeneous soils. This behaviour is due to the fact that the skirt-soil stiffness ratio J is fixed at $z = D$, so that the homogeneous and non-homogeneous soils have the same shear modulus and J at $z = D$, but J is greater in the non-homogeneous soil that in the homogeneous soil for $z < D$ and vice versa when $z > D$. Therefore, given that the skirt mostly behaves as rigid for $J > 20$ [46, 47], all the kinematic interaction factors for non-homogeneous soils and $H/D \leq 1$ are greatly independent from the J and t/D values studied. On the other hand, for $H/D = 2$ it is observed that the kinematic interaction factors depends more on these because J are smaller in the non-homogeneous case than in the homogeneous case when $z > D$.

In summary, when the kinematic interaction factors are presented in dimensionless terms, as it is done here, the responses are relatively insensitive to the skirt–soil stiffness ratio J and the thickness-to-diameter ratio t/D. The differences between the results for the different configurations grow for increasing frequencies and for increasing embedment ratios, being such differences negligible for low frequencies, especially in the case of the non-homogeneous soil. It is also worth noting that the situation of the peaks and troughs of both the real and the imaginary parts of the functions are not significantly shifted in frequency in most cases. At the same time, the natural frequencies of offshore wind turbines tend to be very low (with values well below 0.2 and 2.0 Hz, for instance, for the first and second fore-aft or side-to-side modes), and the energy content of the earthquakes usually decrease for larger frequencies. For these reasons, it could be possible to consider one single curve per embedment ratio, which could be then applied to most of the cases that can be defined within the ranges included in this study, when the combination of properties is such that the most relevant frequency range corresponds to the lower range of the presented dimensionless frequencies.

4.2 Skirt kinematic stresses

The behaviour of the kinematic stresses that arise in the skirt is studied in this section. For the sake of brevity, results are presented only for the representative case of a foundation with a skirt–soil stiffness ratio of $J = 100$ and a thickness ratio of $t/D = 0.01$ in a homogeneous soil, whose response is representative of the response of all of the cases studied.

Figure 9 summarizes the naming conventions that will be used in this section when describing the results. The shell local axis x' is defined as parallel to the global z axis along the whole skirt, while the local axis z' is pointing outwards, with $z' = 0$ being located at the midsurface of the shell. The usual shell stress resultants naming conventions, as described in the figure, are employed for locally describing the stress state. Taking into account that the vertically-incident S wave produces displacements along the y direction, the most relevant locations of the bucket skirt are the two cut lines parallel to the z axis that are highlighted in Figure 9 with thick black lines:

- Cut line at $x = 0$ and $y = D/2$, where the maximum normal stresses occur. Due to the symmetry of the response, only $N_{x'}$, $N_{y'}$, $M_{x'}$, $M_{y'}$ and $V_{x'}$ are non-zero.

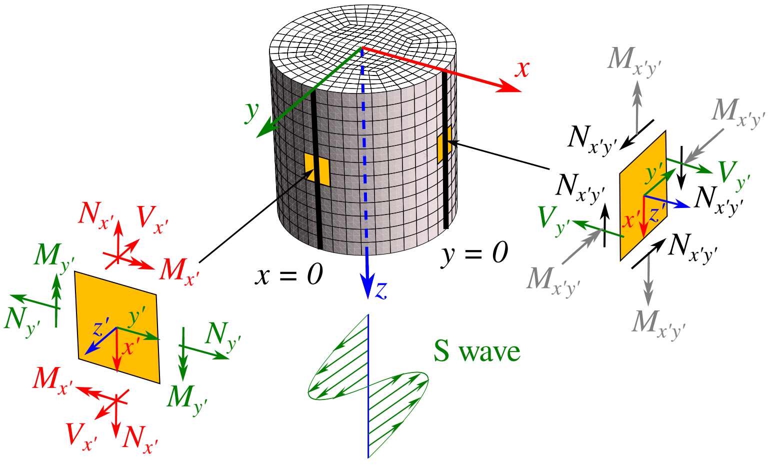

Figure 9: Local axes and stress resultants at relevant locations

- Cut line at $y = 0$ and $x = D/2$, where the maximum tangential stresses occur. Due to the symmetry of the response, only $N_{x'y'}$, $M_{x'y'}$ and $V_{y'}$ are non-zero.

The distribution of the stress resultants around the skirt is complex as it varies from case to case and with the frequency. The choice of the mentioned cut lines for analyzing the stresses are based on establishing reasonable fixed locations where maximum stress resultants are present in most of the cases. In order to illustrate how the different stress resultants vary around the skirt, Fig. 10 shows these for a given case of $H/D = 1$ at $z = D/2$ and at an intermediate frequency $a_0 = 5$. Stress resultants are expressed in dimensionless terms in a way that allow being compared in terms of stresses (it is explained afterwards). It is observed that $N_{x'}$, $N_{y'}$, $M_{x'}$, $M_{y'}$ and $V_{x'}$ have maximum absolute values at $y = D/2$, and zero values at $y = 0$. On the other hand, $N_{x'y'}$, $M_{x'y'}$ and $V_{y'}$ reach maximum absolute values at $y = 0$, while they become null at $y = D/2$. These results show that even though it is a shallow structure ($H/D = 1$) and the skirt have a complex stress state, if the skirt is seen as a beam with rigid circular hollow cross section, then the "beam" normal stresses (role played by $N_{x'}$) follow the plane section hypothesis, i.e. linear distribution of stresses with respect to the neutral axis, and the "beam" tangential stresses (role played by $N_{x'y'}$) follow a parabolic distribution of stresses. The other stress resultants distributions are a consequence of the intrinsic shell behaviour of the skirt, where the circular hollow cross section of the "beam" is obviously not rigid.

4.2.1 Stresses along z at cut line at $x = 0$ and $y = D/2$

The normal stresses $\sigma_{x'}$ and $\sigma_{y'}$ along the cut line at $x = 0$, $y = D/2$ can be obtained as

$$\sigma_{x'} = \frac{N_{x'}}{t} - \frac{M_{x'}}{t^3/12} z' \tag{23}$$

$$\sigma_{y'} = \frac{N_{y'}}{t} - \frac{M_{y'}}{t^3/12} z' \tag{24}$$

These can be expressed at the external and internal faces of the skirt ($z' = \pm t/2$) in dimensionless form as

$$\frac{\sigma_{x'}\left(z' = \pm t/2\right)}{E_{\text{skirt}}} = \frac{N_{x'}}{E_{\text{skirt}} t} \mp \frac{6 M_{x'}}{E_{\text{skirt}} t^2} \tag{25}$$

$$\frac{\sigma_{y'}\left(z' = \pm t/2\right)}{E_{\text{skirt}}} = \frac{N_{y'}}{E_{\text{skirt}} t} \mp \frac{6 M_{y'}}{E_{\text{skirt}} t^2} \tag{26}$$

that would represent the maximum and minimum normal stresses at those surfaces. Likewise, the maximum shear stress produced by the shear force $V_{x'}$ at $z' = 0$ can be expressed as

$$\sqrt{3}\frac{\tau_{x'z'}}{E_{\text{skirt}}} = \sqrt{3}\frac{3}{2}\frac{V_{x'}}{E_{\text{skirt}} t} \tag{27}$$

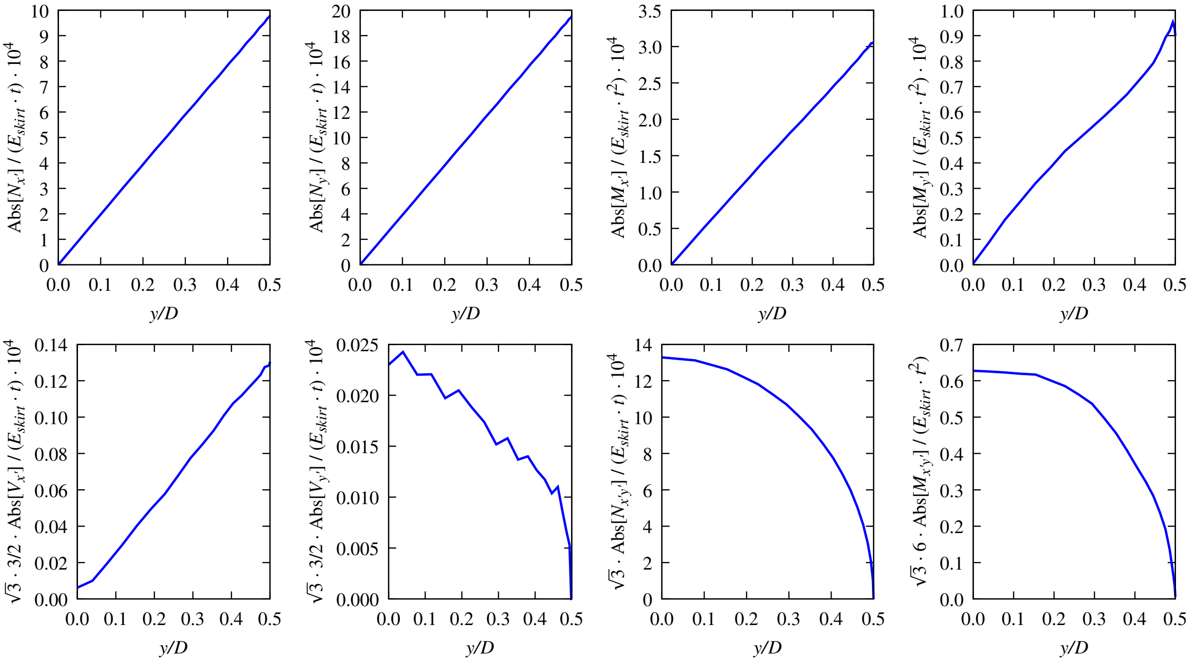

Figure 10: Absolute values of the dimensionless stress resultants around the skirt at $z = D/2$ and at frequency $a_0 = 5$ for the case $H/D = 1$, $J = 100$, $t/D = 1\%$ and homogeneous soil.

where the factor $\sqrt{3}$ is used to enable the comparison between the contributions of normal and shear stresses based on the von Mises yield criterion.

Taking these expressions into account, Figures 11 to 14 present the real and imaginary parts of the three types of summands presented in equations (25) to (27) with respect to the dimensionless frequency a_0. At each figure, the top row presents the contribution of the axial force $N_{x'}$ and bending moment $M_{x'}$ to the normal $\sigma_{x'}\left(z' = \pm t/2\right)/E_{\text{skirt}}$ (Eq. (25)), the middle row presents the contribution of the axial force $N_{y'}$ and bending moment $M_{y'}$ to the normal stress $\sigma_{y'}\left(z' = \pm t/2\right)/E_{\text{skirt}}$ (Eq. (26)), and the bottom row presents the contribution of the shear force $V_{x'}$ to the shear stress $\tau_{x'z'}/E_{\text{skirt}}$ component (Eq. (27)). The range of the color plots is common to all subplots, so that the relative importance of each stress resultant along the depth and with the frequency is clearly identified. The real and imaginary parts represent, in all cases, the components of the complex-valued response that are in phase, or 90 degrees out of phase, respectively, with respect to the peak horizontal free-field displacement produced by the impinging waves at ground surface. Therefore, for any given depth and frequency, the amplitude of the response could be obtained as the modulus of such vector. As can be seen in the color scale shown at the bottom of each figure, the green colors represent small amplitudes in the response, while the peak responses are represented by intense red and blue colors.

Several relevant trends can be observed in these plots. Firstly, the contribution of the shear stress $\tau_{x'z'}$ produced by the shear force $V_{x'}$ is negligible when compared to normal stresses in all cases, even for the highest values of $\tau_{x'z'}$, which are located at the bottom part of the skirt. In contrast, the stress resultant that contribute the most to the total stresses tend to be the bending moments around the axis perpendicular to the seismic shaking, $M_{x'}$, and the axial force parallel to this same direction, $N_{y'}$.

Regarding normal stresses and the structural response for increasing slenderness ratios, there are several observations that can be made on how the skirt responds to the seismic action depending on the skirt depth to diameter ratio. In the cases of shallow buckets ($H/D = 0.25$ and $H/D = 0.5$), whose response is shown in Figures 11 and 12, the $\sigma_{x'}$ normal stress is mainly produced by the $M_{x'}$ bending moment, and the maximum values are located at around 80% depth of the skirt. The $\sigma_{y'}$ normal stress is fundamentally produced by the $N_{y'}$ axial force, and the maximum values occur at the bottom part of the skirt. Of the two, the most important normal stress is clearly $\sigma_{y'}$, showing that the potential seismic failure of this shallow buckets is related to the circumferential stresses at the skirt bottom.

In the cases of normal and moderately deep buckets ($H/D = 1$ and $H/D = 2$), whose response is shown in Figures 13 and 14, there is a change of behaviour of the skirt. First, the $\sigma_{x'}$ normal stress is produced mainly by the $N_{x'}$ axial force in most of the skirt for $H/D = 2$, except at the bottom of the skirt (90% to 95% depth) where the $M_{x'}$ bending moment dominates. This shows that, when the ratio H/D goes beyond the unity, the mid the part of the skirt starts to behave as a circular hollow section beam. Regarding $\sigma_{y'}$ normal stress, the $N_{y'}$ axial force remains as the dominant part. However, now both $\sigma_{x'}$ and $\sigma_{y'}$ are equally important, being $\sigma_{y'}$ more important at the skirt bottom and $\sigma_{x'}$ at the mid part of the skirt. It is also observed that the stress resultants related to the response of the skirt as a cylindrical shell ($M_{x'}$ and $N_{y'}$) are much less relevant for $a_0 < \pi$ than for $a_0 > \pi$. This cut-off frequency ($a_0 \approx \pi$) corresponds with the frequency for which the wavelength λ_s in the soil coincides with the diameter of the skirt (note that $\lambda_s/D = \pi/a_0$). This behaviour illustrates that, as it is physically expected, for $\lambda_s < D$, the structure responds fundamentally through shell vibrations, while for $\lambda_s > D$, the whole skirt starts to behave as a beam. Also, the representation provided in this Figure in terms of modulus of the functions complements those representations given in Figures 11 to 14 in terms of real and imaginary parts. Those figures showed that both parts followed similar trends of rapid variation in frequency that, in contrast, give rise to more clear patterns when presented in form of the absolute value, with the stresses concentrated in the bottom part of the skirt.

This evolution, for increasing slenderness ratios, of the terms that contribute to the $\sigma_{x'}$ and $\sigma_{y'}$ stresses is illustrated more clearly in Figure 15. The upper part of the figure presents the absolute values of the two terms that contribute to $\sigma_{x'}$ (i.e., $|N_{x'}/(E_{\text{skirt}}t)|$ and $|M_{x'}/(E_{\text{skirt}}t^2)|$, on the left and right of each pair of plots), and the lower part of the figure presents the absolute values of the two terms that contribute to $\sigma_{y'}$ (i.e., $|N_{y'}/(E_{\text{skirt}}t)|$ and $|M_{y'}/(E_{\text{skirt}}t^2)|$, on the left and right of each pair of plots). In each case, the color maps for each slenderness ratio are presented keeping the proportions in height, so that the distributions of efforts along the vertical direction can now be directly compared among foundations. The plots illustrate very clearly how the largest kinematic stresses appear always at the bottom part of the foundations, especially in the case of the stresses associated to $M_{x'}$ and $N_{x'}$. They also show that the vertical axial forces $N_{x'}$ are relevant only in the most slender foundation $H/D = 2$, when the structure starts to behave as a beam.

In order to further illustrate this last observation, additional results for the case of a foundation with a much larger slenderness ratio of $H/D = 5$ are also presented in Figure 16. In this case, which is more representative of a monopile than of a bucket, it is clearly observed that the longitudinal axial force $N_{x'}$ becomes the most relevant internal force, illustrating the fact that, as expected, with an increasing slenderness ratio, vertical axial forces $N_{x'}$ continues to gain relevance while the foundation behave increasingly as a beam, in addition to its shell-like response.

4.2.2 Stresses along z at cut line at $y = 0$ and $x = D/2$

In is also relevant to study what happens at the cut made to the cylinder by the xz plane at $x = 0$. Now, the shear stress $\tau_{x'y'}$ along the line at $x = 0$, $y = D/2$ can be obtained as

$$\tau_{x'y'} = \frac{N_{x'y'}}{t} - \frac{M_{x'y'}}{t^3/12} z' \tag{28}$$

which can be expressed, at the external and internal faces of the skirt ($z' = \pm t/2$) in dimensionless form as

$$\sqrt{3}\frac{\tau_{x'y'}\left(z' = \pm t/2\right)}{E_{\text{skirt}}} = \sqrt{3}\frac{N_{x'y'}}{E_{\text{skirt}}t} \mp \sqrt{3}\frac{6M_{x'y'}}{E_{\text{skirt}}t^2} \tag{29}$$

that would represent the maximum and minimum shear stresses at those surfaces. Likewise, the maximum shear stress produced by the shear force $V_{y'}$ at $z' = 0$ can be expressed as

$$\sqrt{3}\frac{\tau_{y'z'}}{E_{\text{skirt}}} = \sqrt{3}\frac{3}{2}\frac{V_{y'}}{E_{\text{skirt}}t} \tag{30}$$

Thus, Figures 17 to 20 present the real and imaginary parts of the five types of summands presented in equations (29) and (30) along the cut at $y = 0$, $x = D/2$, as a function of the dimensionless frequency a_0. At each figure, the top row presents the contribution of the shear force $N_{x'y'}$ and the twisting moment $M_{x'y'}$ to the shear stress $\tau_{x'y'}\left(z' = \pm t/2\right)/E_{\text{skirt}}$ (Eq. (29)), and the bottom row presents the contribution of the shear force $V_{y'}$ to the shear stress $\tau_{y'z'}/E_{\text{skirt}}$ component (Eq. (30)). These three stress resultants ($N_{x'y'}$, $M_{x'y'}$ and $V_{y'}$) produce only shear stress along this cut. The range of the color plots is common to all subplots, so that the relative importance of each stress resultant along the depth and with the frequency is clearly identified.

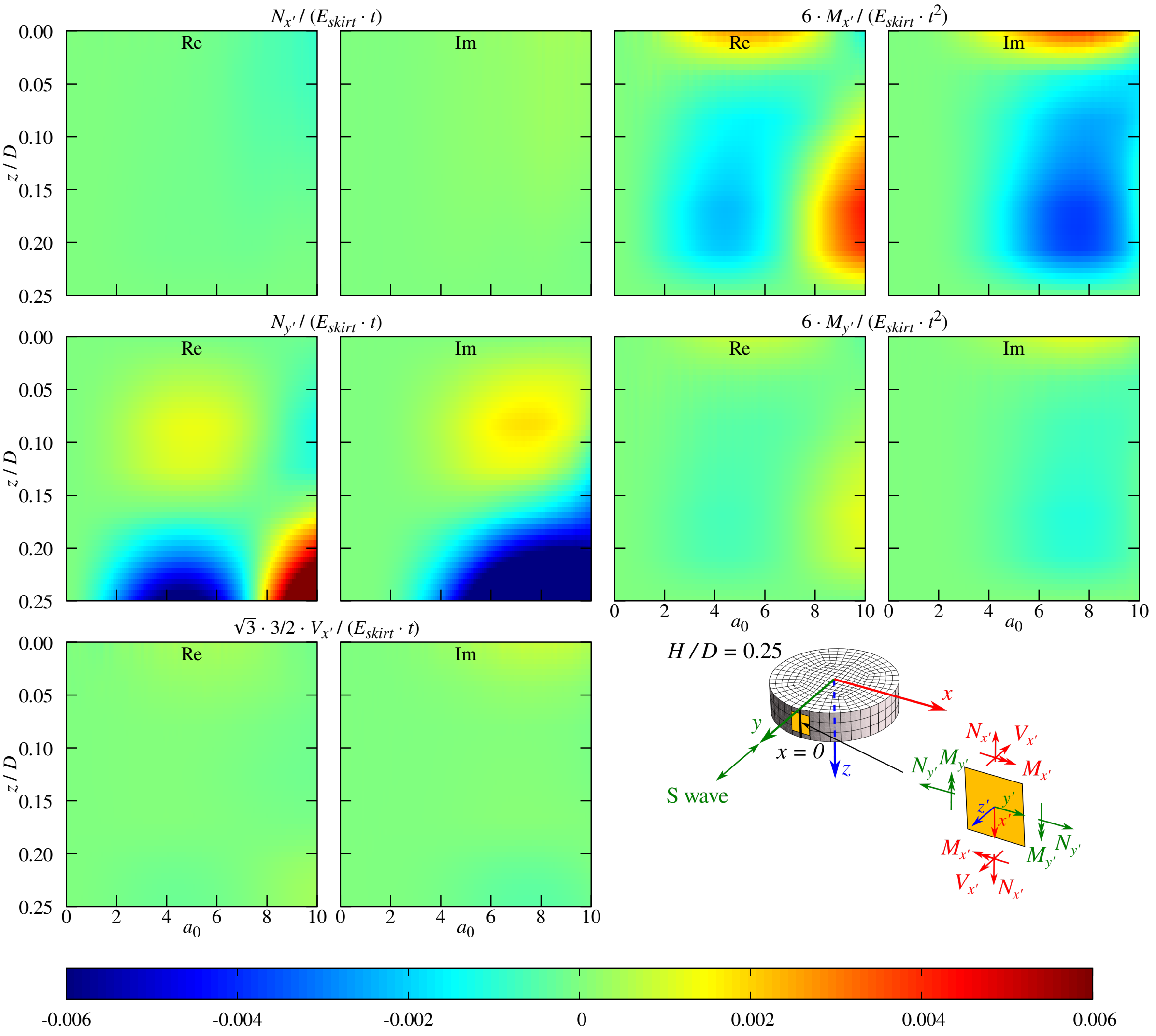

Figure 11: Real and imaginary parts of the dimensionless $N_{x'}$, $M_{x'}$, $N_{y'}$, $M_{y'}$ and $V_{x'}$ along the $x = 0$, $y = D/2$ cut for the case $H/D = 0.25$, $J = 100$, $t/D = 0.01$, and homogeneous soil.

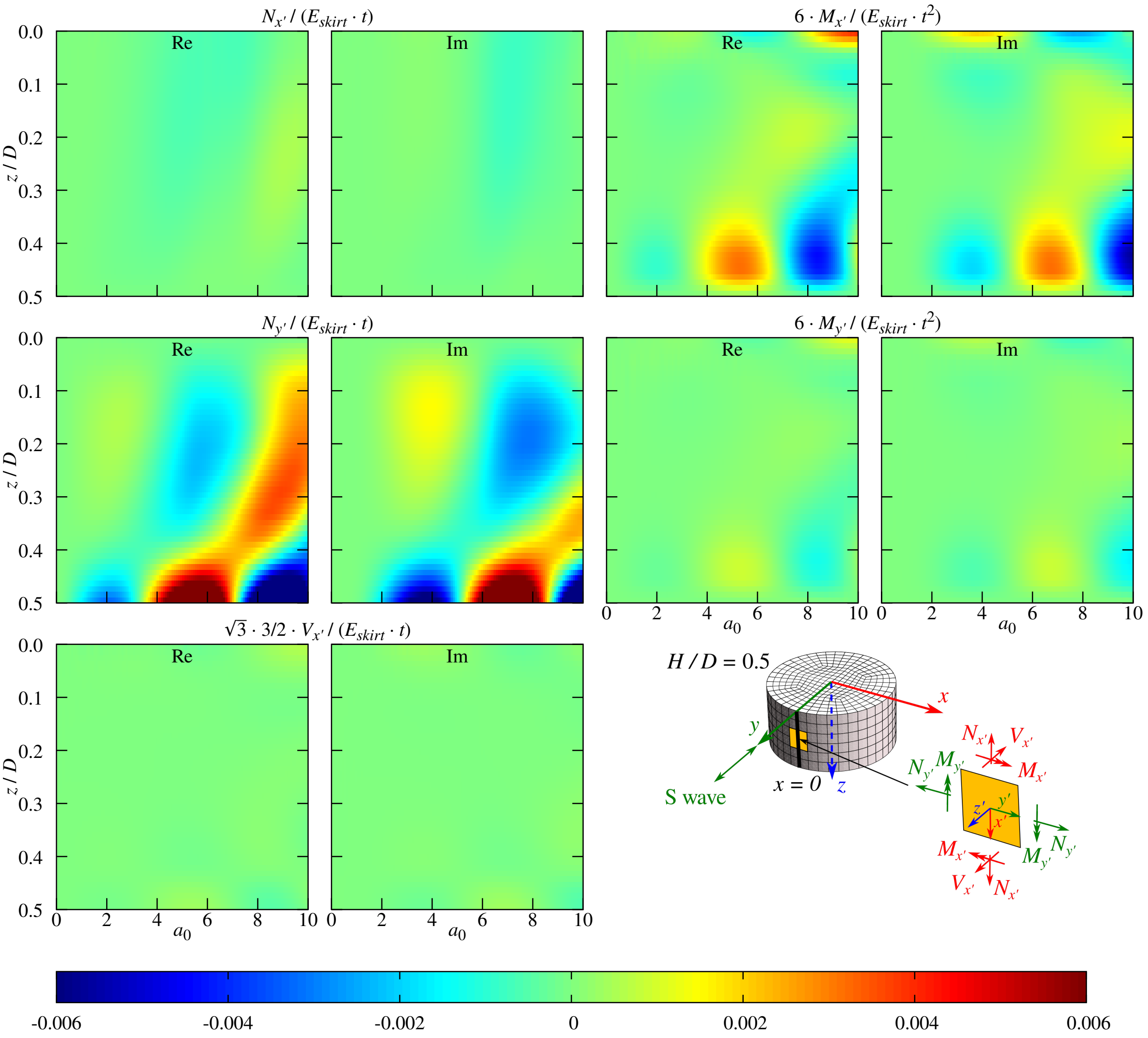

Figure 12: Real and imaginary parts of the dimensionless $N_{x'}$, $M_{x'}$, $N_{y'}$, $M_{y'}$ and $V_{x'}$ along the $x = 0$, $y = D/2$ cut for the case $H/D = 0.5$, $J = 100$, $t/D = 0.01$, and homogeneous soil.

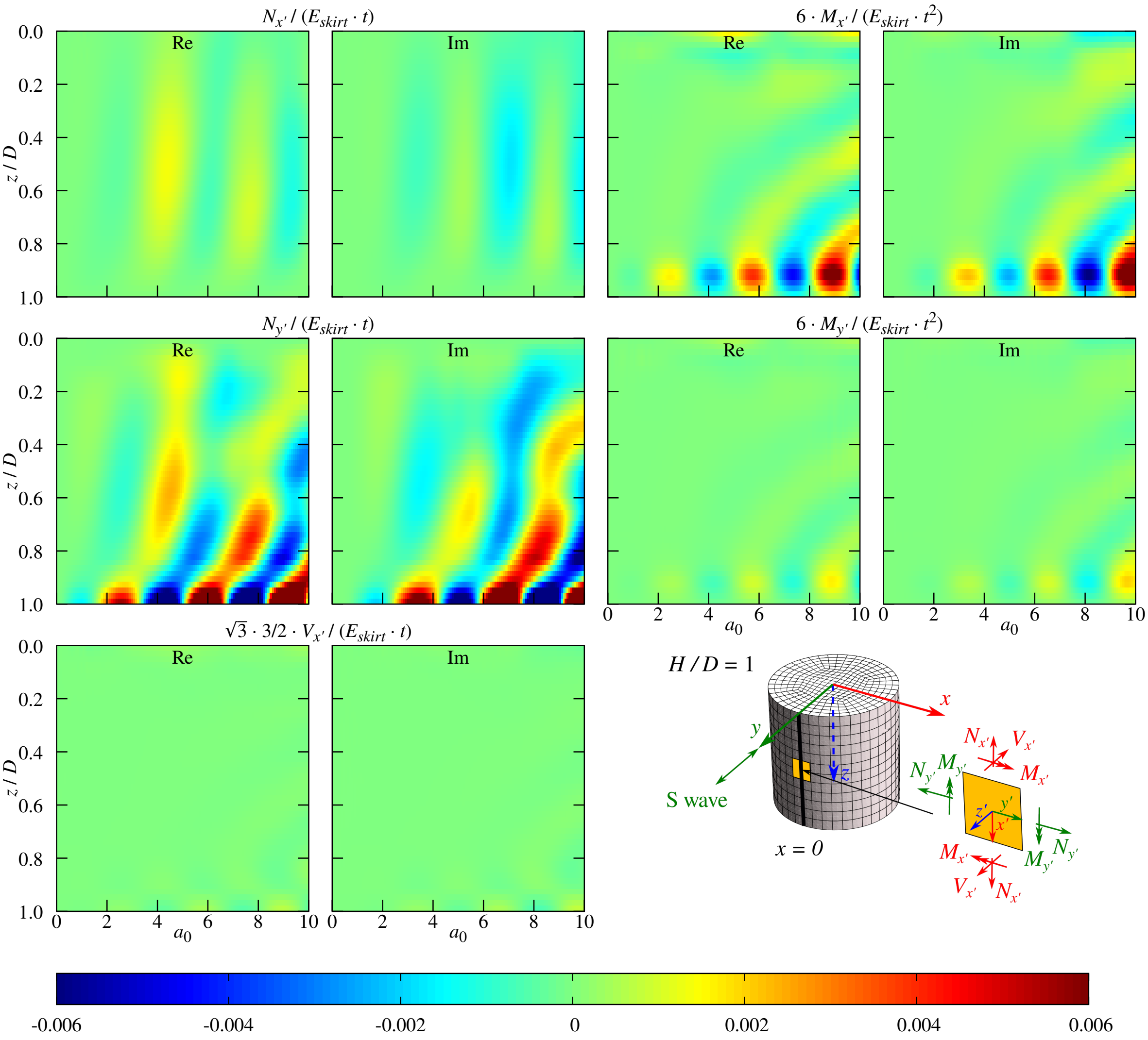

Figure 13: Real and imaginary parts of the dimensionless $N_{x'}$, $M_{x'}$, $N_{y'}$, $M_{y'}$ and $V_{x'}$ along the $x = 0$, $y = D/2$ cut for the case $H/D = 1$, $J = 100$, $t/D = 0.01$, and homogeneous soil.

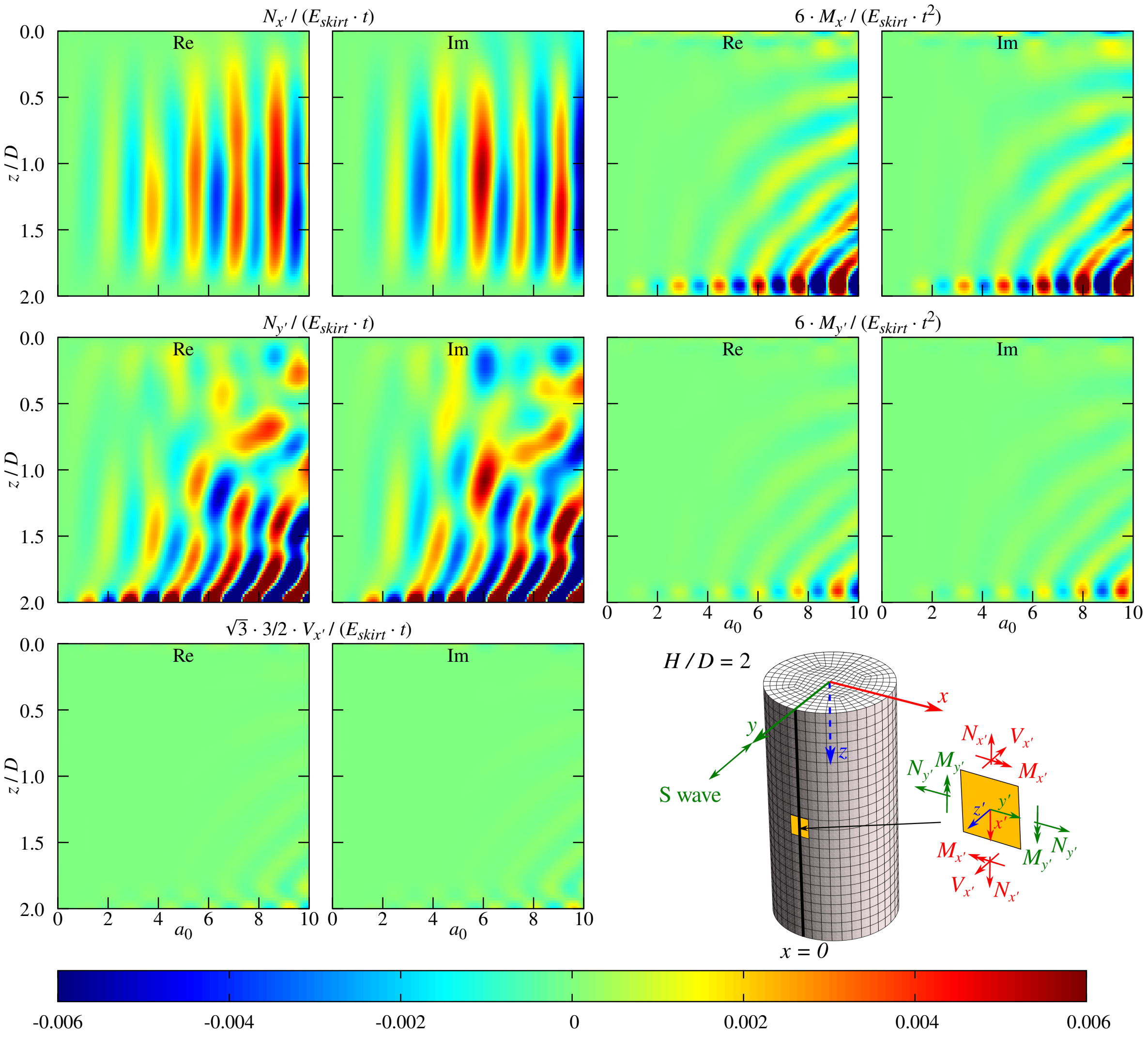

Figure 14: Real and imaginary parts of the dimensionless $N_{x'}$, $M_{x'}$, $N_{y'}$, $M_{y'}$ and $V_{x'}$ along the $x = 0$, $y = D/2$ cut for the case $H/D = 2$, $J = 100$, $t/D = 0.01$, and homogeneous soil.

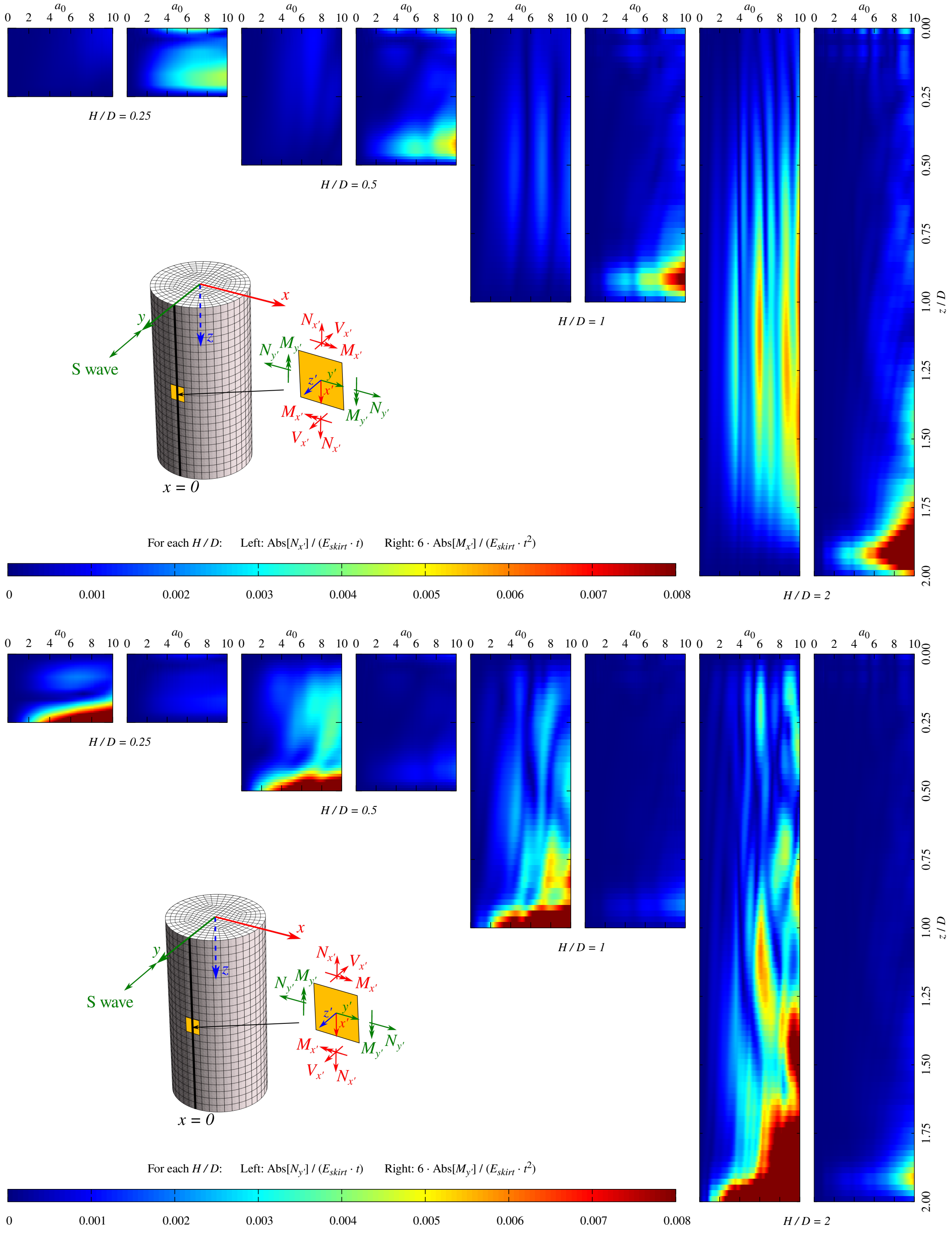

Figure 15: Comparison of the distribution of the absolute values of $N_{x'}$ and $M_{x'}$ (top plots) and $N_{y'}$ and $M_{y'}$ (bottom plots) in dimensionless terms along the $x = 0$, $y = D/2$ cut, for the different slenderness ratios considered. $J = 100$, $t/D = 0.01$, homogeneous soil.

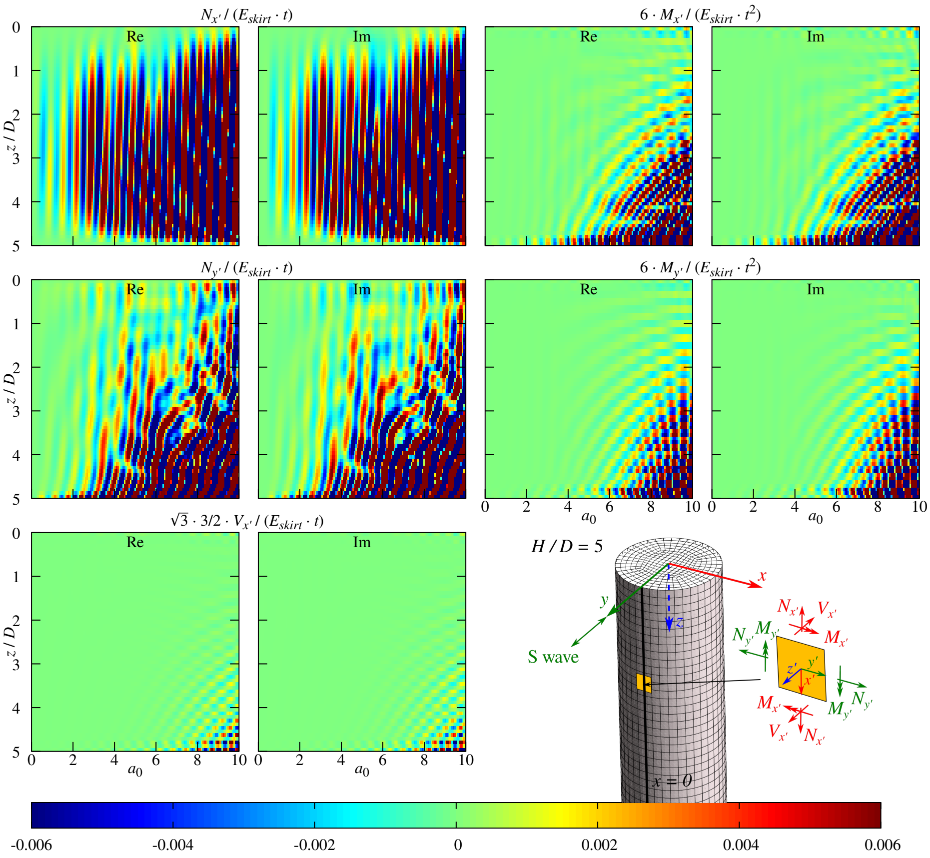

Figure 16: Real and imaginary parts of the dimensionless $N_{x'}$, $M_{x'}$, $N_{y'}$, $M_{y'}$ and $V_{x'}$ along the line at $x = 0$ and $y = D/2$ for the case $H/D = 5$, $J = 100$, $t/D = 0.01$, and homogeneous soil.

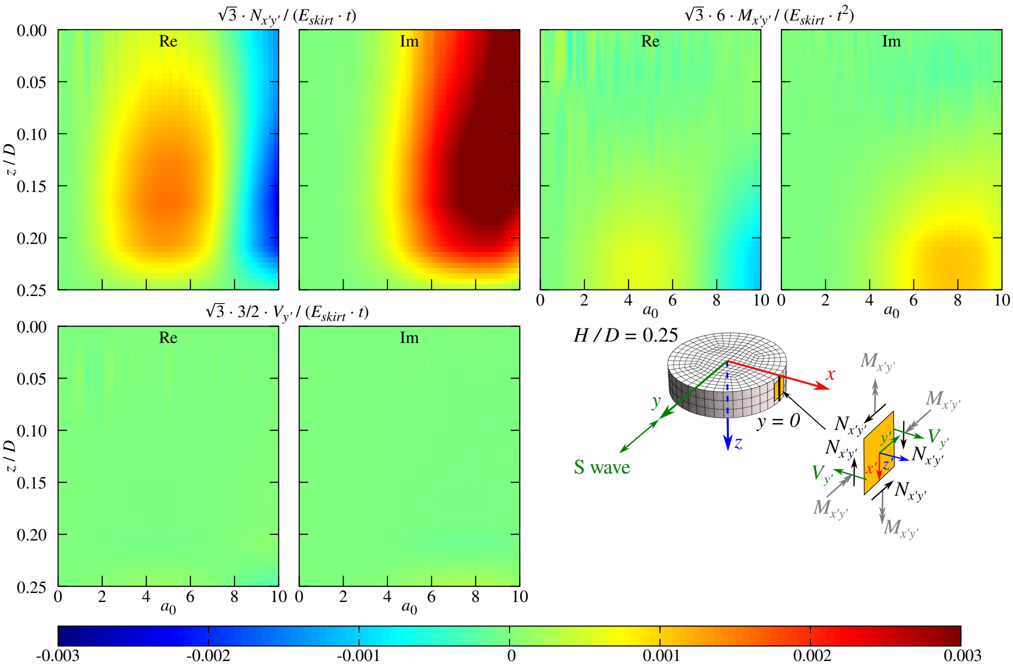

Figure 17: Real and imaginary parts of the dimensionless $N_{x'y'}$, $M_{x'y'}$ and $V_{y'}$ along the line at $y = 0$ and $x = D/2$ for the case $H/D = 0.25$, $J = 100$, $t/D = 0.01$, and homogeneous soil.

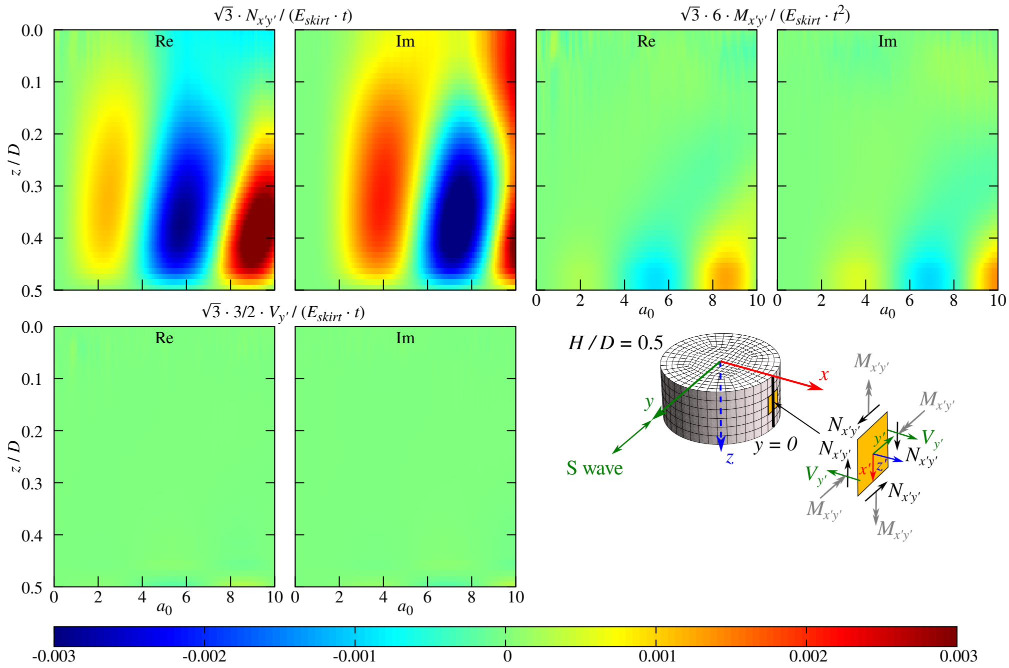

Figure 18: Real and imaginary parts of the dimensionless $N_{x'y'}$, $M_{x'y'}$ and $V_{y'}$ along the line at $y = 0$ and $x = D/2$ for the case $H/D = 0.5$, $J = 100$, $t/D = 0.01$, and homogeneous soil.

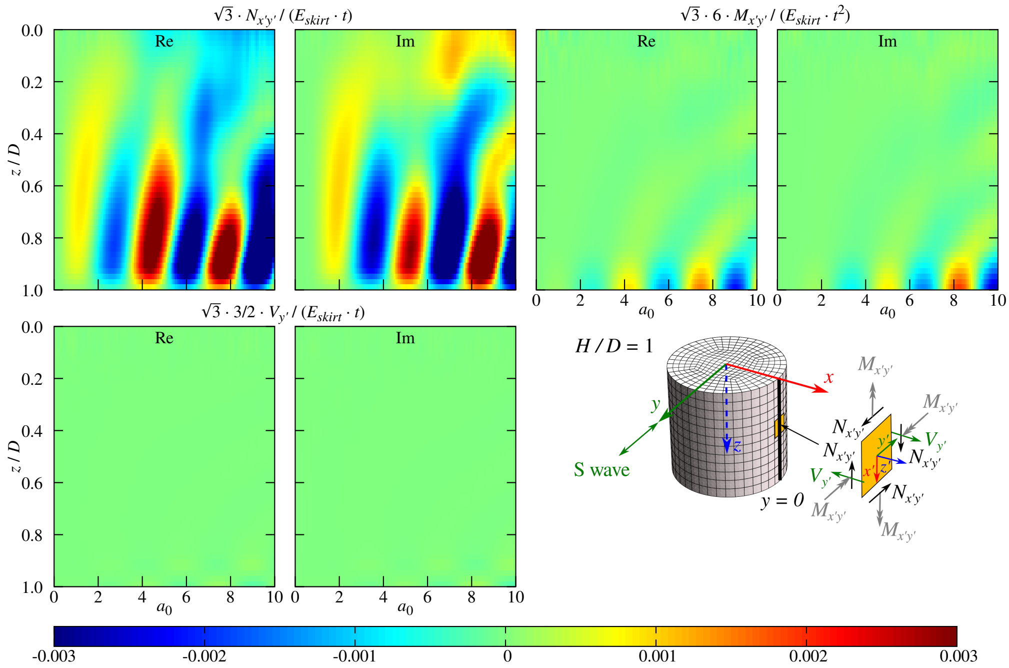

Figure 19: Real and imaginary parts of the dimensionless $N_{x'y'}$, $M_{x'y'}$ and $V_{y'}$ along the line at $y = 0$ and $x = D/2$ for the case $H/D = 1$, $J = 100$, $t/D = 0.01$, and homogeneous soil.

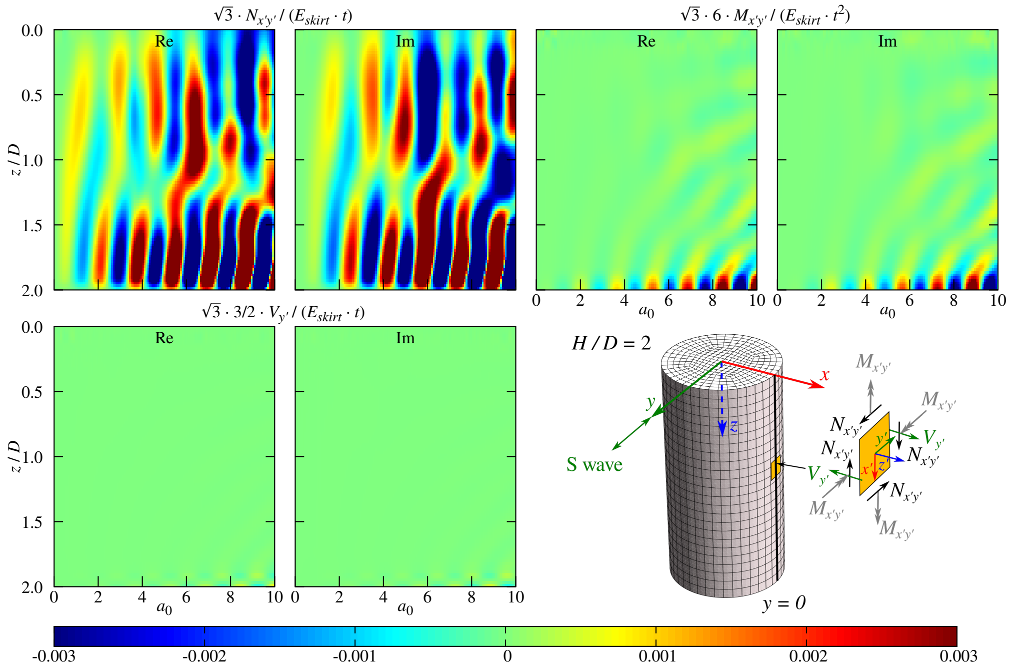

Figure 20: Real and imaginary parts of the dimensionless $N_{x'y'}$, $M_{x'y'}$ and $V_{y'}$ along the line at $y = 0$ and $x = D/2$ for the case $H/D = 2$, $J = 100$, $t/D = 0.01$, and homogeneous soil.

It is observed that the twisting moment $M_{x'y'}$ and the shear force $V_{y'}$ are clearly negligible when compared to the membrane shear force $N_{x'y'}$ in all cases. The twisting moment $M_{x'y'}$ only becomes relevant at the bottom part of the skirt at the higher depth to diameter ratios. The shear force $N_{x'y'}$ reach maximum values at the lower half of the skirt, but is relevant along the whole length. This is seen more clearly in Figure 21, where the absolute values of the twisting moment $M_{x'y'}$ and of the shear force $N_{x'y'}$ are presented for all four slenderness ratios side by side, in the same format used for Figure 15. This representation allows to see that the shear stresses at $y = 0$ are of the same order of magnitude as the normal stresses at $x = 0$, although the peak values does not arise in exactly the same parts of the skirt in both cases.

5 Conclusions

This work has aimed to provide rotational and translational kinematic interaction factors for a foundation configuration for which they were not yet present in the literature. To this end, the kinematic interaction factors of flexible suction caissons subjected to vertically–incident planar shear waves have been computed using a boundary elements – finite elements coupled model that takes into account the real flexibility of the skirt, the soil–skirt and the soil–lid interaction, the three–dimensionality of the problem and the boundless nature of the soil. The translational and the rotational components of the function have been obtained considering ranges of soil and structural properties relevant to the problem of the seismic response of suction caissons as foundations for offshore wind turbines with only one support. Real and imaginary parts of these functions are provided in the frequency range of interest for the seismic analysis of this type of structures. Results are provided for a range of embedment ratios H/D from 0.5 to 2.0, for a thickness ratio t/D of 0.5%, 1.0% and 2.0%, and for homogeneous and non-homogeneous (continuously varying) soils.

It is shown that, when presented in a dimensionaless format, these functions are fundamentally independent of the soil–skirt stiffness ratio J for the ranges of frequencies, and of soil and structural properties, relevant to the problem at hand. It is also shown that the general patterns of the kinematic response of this type of foundation is analogous to that of the monopile, even though the embedment ratios of this last typology is much larger. It is also shown that this type of foundation presents capacity to filter the input seismic signal, especially in the case of soft soils and large–diameter buckets, which should not be an uncommon situation in the case of offshore wind turbines.

These translational and rotational kinematic factors of flexible suction caissons are presented in ready–

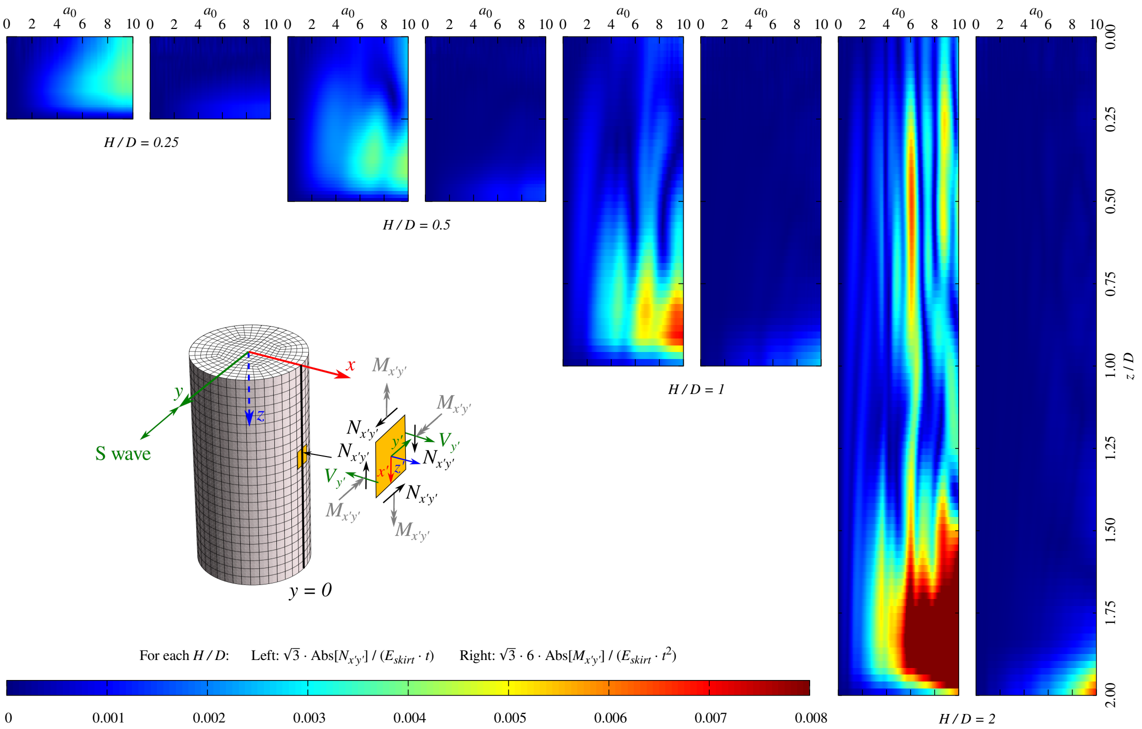

Figure 21: Comparison of the distribution of the absolute values of $N_{x'}$ and $M_{x'}$ in dimensionless terms along the $y = 0$, $x = D/2$ cut, for the different slenderness ratios considered. $J = 100$, $t/D = 0.01$, homogeneous soil.

to–use dimensionless charts that can be easily employed in the analysis of the seismic response of these systems, for instance, when filtering the seismic input to be applied to the foundation of the system in numerical models of the whole turbine.

The manuscript has also presented and analyzed the kinematic stresses developed along the bucket skirt due to the action of the incident seismic S waves. The stresses at two different cuts of the skirt are decomposed into the contributions of the internal forces and moments that arise in the shell structure. It is shown that the largest kinematic stresses tend to arise at the bottom part of the foundations, although in the most slender cases ($H/D \geq 2$), significant stresses appear along the whole length of the skirt because, in such cases, the foundation starts to resist the incoming waves working also as a hollow–section monopile, or beam. It is also worth noting that stresses increase abruptly at frequencies for which the soil wavelength becomes shorter than the diameter of the foundation ($a_0 \approx \pi$).

The results presented in the paper correspond exclusively to the response of the foundations under vertically incident shear waves. However, vertical components of the seismic excitation [55–58] can also be very relevant to the structural integrity of the superstructure. For this reason, kinematic interaction factors corresponding to obliquely incident seismic waves should also be studied in the future together with the effect of foundation-soil-foundation interaction in the case of groups of suction caissons.

Acknowledgements

This research was funded by the Ministerio de Ciencia, Innovación y Universidades and the Agencia Estatal de Investigación of Spain (MCIN/AEI/ 10.13039/501100011033) and FEDER through research project PID2020-120102RB-I00.

References

[1] Eduardo Kausel, Robert V Whitman, Joseph P Morray, and Farid Elsabee. The spring method for embedded foundations. *Nuclear Engineering and Design*, 48(2-3):377–392, August 1978.

[2] George Mylonakis, S Nikolaou, and George Gazetas. Footings under seismic loading: Analysis and design issues with emphasis on bridge foundations. *Soil Dyn Earthquake Eng*, 26(9):824–853, 2006.

[3] Riccardo Conti, Marco Morigi, and Giulia M B Viggiani. Filtering effect induced by rigid massless embedded foundations. *Bulletin of Earthquake Engineering*, 15:1019–1035, 2016.

[4] George Gazetas. Seismic response of end-bearing single piles. *International Journal of Soil Dynamics and Earthquake Engineering,*, 3(2):82–93, 1984.

[5] A M Kaynia and M Novak. Response of pile foundations to Rayleigh waves and obliquely incident body waves. *Earthquake Eng Struct Dyn*, 21:303–318, 1992.

[6] M Kavvadas and G Gazetas. Kinematic seismic response and bending of free-head piles in layered soil. *Géotechnique*, 43(2):207–222, 1993.

[7] George Anoyatis, Raffaele Di Laora, Alessandro Mandolini, and George Mylonakis. Kinematic response of single piles for different boundary conditions: Analytical solutions and normalization schemes. *Soil Dynamics and Earthquake Engineering*, 44:183–195, 2013.

[8] Denghui Dai, M. Hesham El Naggar, Ning Zhang, and Zhanbin Wang. Rigorous solution for kinematic response of floating piles to vertically propagating s-waves. *Computers and Geotechnics*, 137:104270, 2021.

[9] Raffaele Cesaro and Raffaele Di Laora. An analytical solution for the filtering effect of piles in two-layer soil. *Soil Dynamics and Earthquake Engineering*, 175:108273, 2023.

[10] S M Mamoon and P K Banerjee. Response of piles and pile groups to travelling sh-waves. *Earthquake Eng Struct Dyn*, 19:597–610, 1990.

[11] K Fan, George Gazetas, A M Kaynia, E Kausel, and S Ahmad. Kinematic seismic response of single piles and pile groups. *J Geotech Eng, ASCE*, 117(12):1860–1879, 1991.

[12] George Gazetas, K Fan, T Tazoh, K Shimizu, M Kavvadas, and N Makris. Seismic pile-group-structure interaction. *Geotech Spec Publ, ASCE*, 34:56–93, 1992.

[13] Cristina Medina, Luis A Padrón, Juan J Aznárez, Ariel Santana, and Orlando Maeso. Kinematic interaction factors of deep foundations with inclined piles. *Earthquake Engineering and Structural Dynamics*, 43:2035–2050, 2014.

[14] Raffaele Di Laora, Yado Grossi, Luca de Sanctis, and Giulia M.B. Viggiani. An analytical solution for the rotational component of the foundation input motion induced by a pile group. *Soil Dynamics and Earthquake Engineering*, 97:424–438, 2017.

[15] Guillermo M Álamo, Juan J Aznárez, Luis A Padrón, Alejandro E Martínez-Castro, and Orlando Maeso. Importance of using accurate soil profiles for the estimation of pile kinematic input factors. *Journal of Geotechnical and Geoenvironmental Engineering*, 145(8):04019035, 2019.

[16] Rui He, Amir M. Kaynia, Jisheng Zhang, and Weiyun Chen. Seismic response of monopiles to vertical excitation in offshore engineering. *Ocean Engineering*, 216:108120, 2020.

[17] Rui He, Amir M. Kaynia, and Jisheng Zhang. Lateral free-field responses and kinematic interaction of monopiles to obliquely incident seismic waves in offshore engineering. *Computers and Geotechnics*, 132:103956, 2021.

[18] Libo Chen, Wenbing Wu, Hao Liu, Jiaxuan Li, Tim Newson, and M. Hesham El Naggar. Analytical solution for kinematic response of offshore piles under vertically propagating S-waves. *Ocean Engineering*, 262:112018, 2022.

[19] Changjie Zheng, Tong Luo, and Lubao Luan. Lateral kinematic response of offshore pipe piles to S-wave seismic excitation. *Numerical and analytical methods in geomechanics*, 47(8):1496–1518, 2023.

[20] S Nikolaou, G Mylonakis, G Gazetas, and T Tazoh. Kinematic pile bending during earthquakes: analysis and field measurements. *Géotechnique*, 51(5):425–440, 2001.

[21] F. Dezi, S. Carbonari, and G. Leoni. Kinematic bending moments in pile foundations. *Soil Dynamics and Earthquake Engineering*, 30(3):119–132, 2010.

[22] Raffaele Di Laora, Alessandro Mandolini, and George Mylonakis. Insight on kinematic bending of flexible piles in layered soil. *Soil Dynamics and Earthquake Engineering*, 43:309–322, 2012.

[23] Raffaele Di Laora, George Mylonakis, and Alessandro Mandolini. Pile-head kinematic bending in layered soil. *Earthquake Engineering and Structural Dynamics*, 42(3):319–337, 2012.

[24] Stefano Stacul, Emmanouil Rovithis, and Raffaele Di Laora. Kinematic soil–pile interaction under earthquake–induced nonlinear soil and pile behavior: An equivalent–linear approach. *Journal of Geotechnical and Geoenvironmental Engineering*, 148(7):04022055, 2022.

[25] Raffaele Di Laora. Kinematic bending of piles in made ground. *Geotechnique*, 2023.

[26] A M Kaynia and S Mahzooni. Forces in pile foundations under seismic loading. *J Eng Mech, ASCE*, 122:46–53, 1996.

[27] Francesca Dezi and Harry Poulos. Kinematic bending moments in square pile groups. *International Journal of Geomechanics*, 17(3):04016066, 2017.

[28] Rosa Maria Stefania Maiorano, Luca De Sanctis, Stefano Aversa, and Alessandro Mandolini. Kinematic response analysis of piled foundations under seismic excitation. *Canadian Geotechnical Journal*, 46(5):571 – 584, 2009.

[29] Jose M Zarzalejos, Juan J Aznárez, Luis A Padrón, and Orlando Maeso. Influence of type of wave and angle of incidence on seismic bending moments in pile foundations. *Earthquake Engineering and Structural Dynamics*, 43:41–59, 2014.

[30] Luis A Padrón, Adrián Suárez, Juan J Aznárez, and Orlando Maeso. Kinematic internal forces in deep foundations with inclined piles. *Earthquake Engineering and Structural Dynamics*, 44:2129–2135, 2015.

[31] Guillermo M Álamo, Luis A Padrón, Juan J Aznárez, and Orlando Maeso. Computation of pile kinematic bending moments in non-homogeneous soil profiles. testing the validity of a simplified vs30-equivalent homogeneous medium. *Soil Dynamics and Earthquake Engineering*, 131:106062, 2020.

[32] C. Latini and V. Zania. Vertical dynamic impedance of suction caissons. *Soils and Foundations*, 59(5):1113–1127, 2019.

[33] Morten Liingaard, Lars Andersen, and Lars Bo Ibsen. Impedance of flexible suction caissons. *Earthquake Engineering and Structural Dynamics*, 36(14):2249–2271, 2007.

[34] Jacob D R Bordón, Juan J Aznárez, and Orlando Maeso. Dynamic model of open shell structures buried in poroelastic soils. *Computational Mechanics*, 60:269–288, 2017.

[35] Saleh Jalbi, Masoud Shadlou, and S. Bhattacharya. Impedance functions for rigid skirted caissons supporting offshore wind turbines. *Ocean Engineering*, 150:21–35, 2018.

[36] Jijian Lian, Qi Jiang, Xiaofeng Dong, Yue Zhao, and Hao Zhao. Dynamic impedance of the wide-shallow bucket foundation for offshore wind turbine using coupled finite–infinite element method. *Energies*, 12(22), 2019.

[37] Kristoffer Skjolden Skau, Hans Petter Jostad, Gudmund Eiksund, and Hendrik Sturm. Modelling of soil-structure-interaction for flexible caissons for offshore wind turbines. *Ocean Engineering*, 171:273–285, 2019.

[38] Georgia Efthymiou and George Gazetas. Elastic stiffnesses of a rigid suction caisson and its cylindrical sidewall shell. *Journal of Geotechnical and Geoenvironmental Engineering*, 145(2), 2019.

[39] J.D.R. Bordón, J.J. Aznárez, L.A. Padrón, O. Maeso, and S. Bhattacharya. Closed-form stiffnesses of multi-bucket foundations for owt including group effect correction factors. *Marine Structures*, 65:326–342, 2019.

[40] AbdelRahman Salem, Saleh Jalbi, and Subhamoy Bhattacharya. Vertical stiffness functions of rigid skirted caissons supporting offshore wind turbines. *Journal of Marine Science and Engineering*, 9(6):573, 2021.

[41] Rui He and Amir M. Kaynia. Dynamic impedances and load carrying mechanism for skirted foundations. *Marine Structures*, 79:103023, 2021.

[42] Soumia Bouneguet, Salah Messioud, and Daniel Dias. Vertical and horizontal dynamic response of suction caisson foundations. *Studia Geotechnica et Mechanica*, 45(1):1 – 13, 2023.

[43] Huishan Li, Jijian Lian, Run Liu, Haijun Wang, and Xu Yang. Research on the equivalent stiffness of bucket foundations for offshore wind power. *Ocean Engineering*, 302:117596, 2024.

[44] Xuyue Wang, Sai Jia, Yuliang Wang, Xinglei Cheng, Ling Wang, and Chuang Cheng. Study on frequency domain impedance of wide-shallow composite bucket foundation for offshore wind turbine. *Ocean Engineering*, 303:117708, 2024.

[45] Sandro Carbonari, Jacob D R Bordón, Luis A Padrón, Michele Morici, Francesca Dezi, Juan J Aznárez, Graziano Leoni, and Orlando Maeso. Winkler model for predicting the dynamic response of caisson foundations. *Earthquake Engineering and Structural Dynamics*, 51(13):2069–3096, 2022.

[46] J. P. Doherty, G. T. Houlsby, and A. J. Deeks. Stiffness of flexible caisson foundations embedded in nonhomogeneous elastic soil. *Journal of Geotechnical and Geoenvironmental Engineering*, 131(12):1498–1508, 2005.

[47] Guillermo M. Álamo, Jacob D.R. Bordón, and Juan J. Aznárez. On the application of the beam model for linear dynamic analysis of pile and suction caisson foundations for offshore wind turbines. *Computers and Geotechnics*, 134:104107, 2021.

[48] Jacob D.R. Bordón, Guillermo M. Álamo, Luis A. Padrón, Juan J. Aznárez, and Orlando Maeso. MultiFEBE: A multi-domain finite element–boundary element solver for linear mixed–dimensional mechanical problems. *SoftwareX*, 20:101265, 2022.

[49] Ronald Y. S. Pak and Bojan B. Guzina. Three-dimensional green's functions for a multilayered half–space in displacement potentials. *Journal of Engineering Mechanics*, 128(4):449–461, 2002.

[50] Miguel Luiz Bucalem and Klaus-Jüen Bathe. Higher-order mitc general shell elements. *International Journal for Numerical Methods in Engineering*, 36(21):3729–3754, 1993.

[51] E. Oñate. *Structural Analysis with the Finite Element Method. Linear Statics.*, volume Volume 2: Beams, Plates and Shells of *Lecture Notes on Numerical Methods in Engineering and Sciences.* Springer Dordrecht, 1st edition edition, 2013.

[52] J. Domínguez. *Boundary Elements in Dynamics.* WIT Press, 1993.

[53] J.D. Achenbach. *Wave propagation in elastic solids.* North-Holland, Amsterdam, 1973.

[54] L.V. Andersen. *Linear elastodynamic analysis.* Department of Civil Engineering, Aalborg. University. DCE Lecture Notes, No. 3, 2006.

[55] Remi A. Kjørlaug and Amir M. Kaynia. Vertical earthquake response of megawatt-sized wind turbine with soil-structure interaction effects. *Earthquake Engineering & Structural Dynamics*, 44(13):2341–2358, 2015.

[56] Amir M. Kaynia. Seismic considerations in design of offshore wind turbines. *Soil Dynamics and Earthquake Engineering*, 124:399–407, 2019.

[57] Hui Zhang Qianqian Ren, Yazhou Xu and Junqi Yu. Seismic performance of a wind turbine tower under near-field vertical earthquake excitation. *Structure and Infrastructure Engineering*, 19(10):1334–1348, 2023.

[58] Piguang Wang, Baoxin Wang, Xinglei Cheng, Mi Zhao, and Xiuli Du. Seismic response of monopile offshore wind turbines in liquefiable sand considering vertical ground motion. *Soil Dynamics and Earthquake Engineering*, 189:109117, 2025.